Progress in and Outlook for Cryogenic Microcooling

H.S. Cao[1,*] and H.J.M. ter Brake[2]

[1]*Key Laboratory for Thermal Science and Power Engineering of Ministry of Education, Department of Energy and Power Engineering, Tsinghua University, Beijing 100084, China*

[2]*Faculty of Science and Technology, University of Twente, Enschede, 7500 AE, Netherlands*

Semiconductor-based devices in various fields such as night vision, space exploration, medical inspection, telecommunication, among others could benefit from operating at cryogenic temperatures. Besides, cryogenic temperatures also can offer some unique capabilities to superconducting devices, which are not available at ambient temperature. However, existing cryocoolers are oversized in terms of size and cooling power. Widespread use of these electronic devices requires cryocoolers that are small, low cost, low interference, and reliable. This review presents an overview of cooling cycles and discusses the opportunities and difficulties when adopting these cycles for realizing cryogenic temperatures above 1 K in microscale. It is found by comparison that, at present, fluid-based cryocoolers are more suitable for miniaturization. Concerning the miniaturization of fluid-based cryocoolers, emphasis is put on the effect that scaling has on the gross and net cooling power and on various parasitic losses, the microscale manufacturing technologies, and the state of the art of microcoolers. Some aspects that remain to be further developed for widespread use of cryogenic microcooling, are considered at the end of this review.

I. BACKGROUND

For a number of electronic devices, colder is better. Electronic devices, such as CMOS Si electronics [1,2], GaAs-based low-noise amplifiers [3], infrared detectors [4], and x-ray detectors [5], could benefit from operating at cryogenic temperatures in several forms: higher speed, higher signal-to-noise ratio, larger bandwidth, improved sensitivity [6]. Cryogenic temperatures also can offer some unique capabilities to superconducting devices [7–9], which are not available at ambient temperature. Besides electronic devices, experimental research on temperature-dependent properties, such as resistance, Seebeck coefficient, mobility, impurity distribution, etc [10], also requires cryogenic temperatures. Figure 1 shows a number of applications in the plane of required cooling power versus requried temperature.

At present, existing cryogenic coolers (cryocoolers) are very large compared to sizes of the applications that require a cooling power less than 1 W and mismatch the small cooling power requirements of these applications. There are a number of applications where the performance improvement gained by cooling is overruled by the effort and complexity of the cryogenic burden caused by relatively large cryocoolers. Widespread use of these

applications requires cryocoolers that have matched size and provide matched cooling power [13,14]. Here, we present a review of the developments on micromachined cryocoolers that have a size smaller than a few centimeters cube, and provide a cooling power in the range of 1–500 mW at a cooling temperature in the range 20–150 K. Miniature cryocoolers have advantages not only in their matched size and cooling power but also in their fast response, which make them attractive for measurements of temperature-dependent properties. The fast response refers to the rapid cool down and warm up of the miniature cryocoolers, which allows measuring the properties of more samples in a shorter time.

In the next section, we present an overview of cooling principles that are most commonly used to provide cryogenic temperatures. The challenges and opportunities of miniaturization of cryocoolers based on these cooling principles are introduced. In Sec. III, the theory and scaling behavior of fluid-based cryocoolers are discussed in detail and suitable measures to realize these cryocoolers in microscale are suggested. Section IV discusses the opportunities and limitations of small-scale manufacturing technologies for fabricating elements of cryogenic systems in microscale. The current status of the miniaturization of fluid-based cryocoolers is reviewed and the corresponding difficulties are summarized in Sec. V. Finally, we discuss several research directions, which could lead to the widespread use of microcooling.

_____

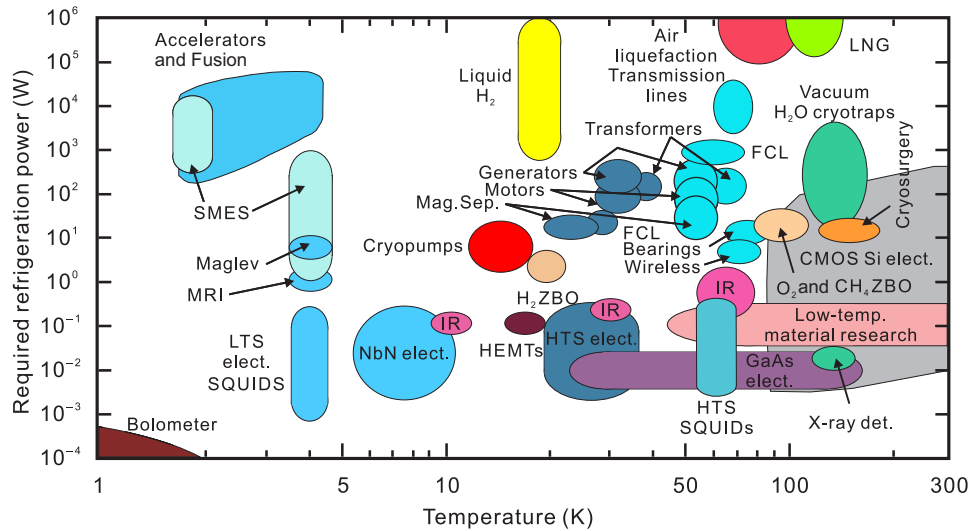*HaishanCao@tsinghua.edu.cn; HaishanCao@gmail.com

FIG. 1.   Cryocooler applications in plane of required refrigeration power versus temperature (adapted from Refs. [11,12]). CMOS Si elect., CMOS silicon electronics; FCL, fault current limiter; GaAs elect., gallium-arsenide electronics; HEMTs, high electron mobility transistors; IR, IR detectors; LNG, liquefied natural gas; Low-temp.mat. res., low-temperature material research; LTS elect., low-temperature superconducting electronics; LTS SQUIDs, low-temperature superconducting quantum interference devices; Maglev, magnetic levitation; Mag. Sep., magnetic separator; MRI, magnetic resonance imaging; NbN elect., NbN electronics; SMES, superconducting magnetic energy storage; X-ray det., x-ray detectors; ZBO, zero boil-off.

II. COOLING PRINCIPLES

Cryocoolers can be broadly classified into two groups based on the state of the working substance, including fluid-based (liquid or gas) cryocoolers and solid-based cryocoolers. The fluid-based cryocoolers rely on compression and expansion of a working fluid to bring about temperature changes, which are classified into recuperative and regenerative cryocoolers. Recuperative cryocoolers, for instance, Joule-Thomson (JT), Brayton and Claude cryocoolers, use a counter-flow heat exchanger (CFHX) to exchange heat between the hot and cold flows. In regenerative cryocoolers, such as Stirling, pulse-tube, and Gifford-McMahon cryocoolers, on the other hand, the working fluid flows back and forth through a regenerator (an arrangement or matrix of solid material).

Instead of using liquid or gas, the solid-based cryocoolers use the thermoelectric effect [15], the magnetocaloric effect [16], the electrocaloric effect [17], and anti-Stokes fluorescence [18] among others, realizing cooling. Thermoelectric cooling is of particular interest for miniaturization, but the achievable temperatures that can be reached from room temperature at reasonable efficiency are far above the cryogenic range. For magnetocaloric cooling, it is challenging to achieve cryogenic temperatures starting from ambient temperatures. Moreover, a strong magnetic field is required, which is still a bottleneck in the miniaturization of magnetocaloric cooling systems. Electrocaloric cooling is analogous to magnetocaloric cooling except that the temperature change in the material is achieved by changing the electric field. In contrast to magnetocaloric

cooling, it is much easier to produce relatively high electric fields in a small size. It is, however, still challenging to design electrocaloric materials for cryogenic applications. Anti-Stokes fluorescence cooling can occur only in special very high-purity materials that have appropriately spaced energy levels. The typical materials for anti-Stokes fluorescence cooling include glasses and crystals doped with rare-earth elements or direct-bandgap semiconductors such as gallium arsenide. To realize anti-Stokes fluorescence cooling in a small size, the following aspects still need to be overcome: enhancement of the absorbed power in small scale, thermally isolating the support for the crystal, thermally linking the device to be cooled to the crystal, and the miniaturization of the laser pump source. To summarize, although these solid-based cooling cycles are attractive for miniaturization, these cycles are currently not suitable for reaching cryogenic temperatures in microscale because of the limits of material properties and further operating conditions. Therefore, this microcooling review is limited to fluid-based cryocoolers.

A. Recuperative cryocooler

In a recuperative cryocooler, the working fluid flows around a loop in one direction. The heat exchanger of a recuperative cryocooler is known as a counter-flow heat exchanger. It has two separate flow channels, a high- and a low-pressure channel. The expansion process from a high pressure to a low pressure can occur through a restriction as in the JT cryocooler or through an expander as in the Brayton cryocooler (see Fig. 2). The Claude cryocoler is
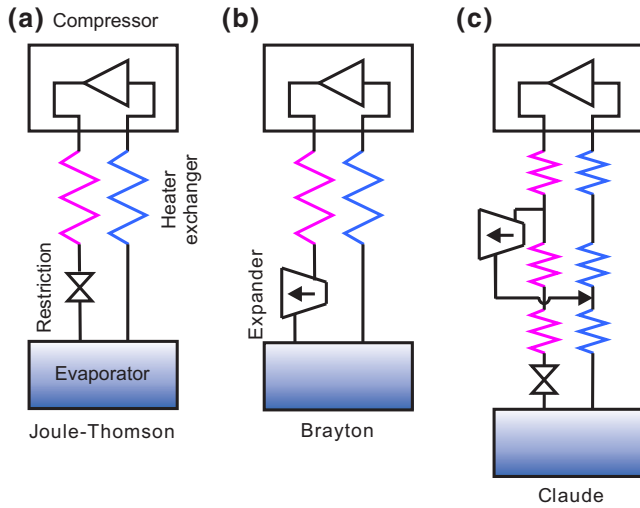
FIG. 2. Schematics of the three most common recuperative cycles.

a combination of the two in which an expander is used for precooling and the JT restriction is used for the final expansion. Differing from a JT cryocooler, both Brayton and Claude cryocoolers have an expander with moving parts at low temperatures.

The cold-end temperatures of recuperative cryocoolers are determined by the boiling temperature of the working fluid in the evaporator. The normal boiling temperatures of commonly used gases are shown in Table I.

The coefficient of performance (COP) of cryocoolers, η, is defined as the ratio between the cooling power $\dot{Q}_c$ and the required compressor power $\dot{W}_0$:

$$\eta = \frac{\dot{Q}_c}{\dot{W}_0}. \tag{1}$$

The gross cooling power of a JT cryocooler is defined by

$$\dot{Q}_{c,\text{JT}} = \dot{m}\Delta h_{\min}, \tag{2}$$

where $\dot{m}$ is the mass-flow rate, $\Delta h_{\min}$ is the minimum value of the isothermal enthaply difference over the temperature between the cold and warm ends of the CFHX of the cryocooler.

The gross cooling power of a Brayton cryocooler is defined by

$$\dot{Q}_{c,\text{Brayton}} = \dot{m}\left(\Delta h_{\min} + w\right), \tag{3}$$

TABLE I. Normal boiling points of different gases [19,20].

Gas	CH$_4$	O$_2$	Ar	CO	N$_2$	Ne	H$_2$
Normal boiling point (K)	111.5	90.1	87.2	81.5	77.2	27.1	20.3

where w is the specific work extracted from the expander.

The gross cooling power of a Claude cryocooler is defined by

$$\dot{Q}_{c,\text{Claude}} = \dot{m}_1 \Delta h_{\min} + \dot{m}_2 w, \tag{4}$$

where $\dot{m}_1$ and $\dot{m}_2$ are the mass-flow rates through the restriction and the expander, respectively.

The required compression work of a compressor is minimum when compression follows the isothermal process, given by

$$\dot{W}_0 = \dot{m}\left\{ h\left(T_h, p_L\right) - h\left(T_h, p_H\right) \right.$$
$$\left. - T_h\left[s\left(T_h, p_L\right) - s\left(T_h, p_H\right)\right]\right\} \tag{5}$$

or

$$\dot{W}_0 = \dot{m}\left[g\left(T_h, p_L\right) - g\left(T_h, p_H\right)\right], \tag{6}$$

where $h\left(T_h, p_L\right)$ and $h\left(T_h, p_H\right)$ are the specific enthalpies of the gas at the outlet and the inlet of the cryocooler, $s\left(T_h, p_L\right)$ and $s\left(T_h, p_H\right)$ are the corresponding specific entropies of the gas, and $g\left(T_h, p_L\right)$ and $g\left(T_h, p_H\right)$ are the corresponding specific Gibbs free energies of the gas. Here T_h is the temperature at the warm end, p_H is the high pressure and p_L is the low pressure.

The expansion process through a restriction in a JT cryocooler is an isenthalpic process, whereas the practical expansion process for an expander is much closer to an isentropic process, producing work output. Therefore, the ideal COP of Brayton and Claude cryocoolers are higher than that of a JT cryocooler.

B. Regenerative cryocooler

A regenerative cryocooler operates with oscillating pressures and mass flows, and the working fluid is usually helium gas. These are extensively discussed in Refs. [20–23]. Cold-end temperatures achieved with regenerative cryocoolers vary from about 3 K up to ambient temperatures. Maximum refrigeration of a regenerative cryocooler occurs when flow and pressure are in phase near the cold end. The phase angle is set by the phase of the displacer with respect to the compressor piston in both the Stirling and Gifford-McMahon (GM) cryocoolers. There is no displacer in the pulse-tube cryocooler and the phase between flow and pressure is set by the flow impedance at the warm end of the pulse-tube cryocooler. Both Stirling and pulse-tube cryocoolers do not need check valves to control the flows, in contrast to GM cryocoolers (see Fig. 3).

The Stirling cycle is comprised of two reversible isothermal and two reversible isochoric processes, and the COP of an ideal Stirling cryocoler, $\eta_{S,\text{ideal}}$, is the Carnot COP, given by

$$\eta_{S,\text{ideal}} = \eta_{\text{Carnot}} = T_c / \left(T_h - T_c\right), \tag{7}$$
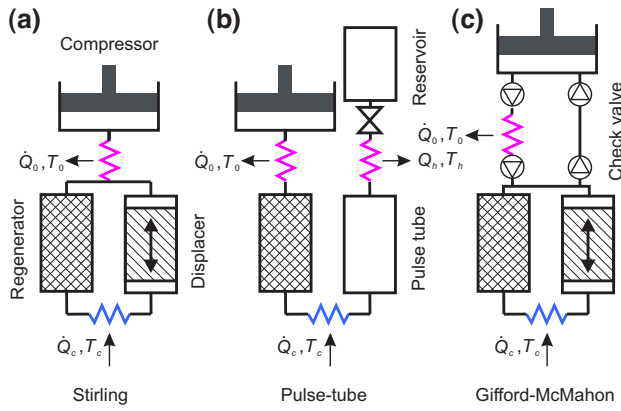
FIG. 3. Schematics of the most common regenerative cycles (adapted from Ref. [21]). The compressor without or with check valves provides the pressure oscillations that drive the cryocooler; the regenerator is a periodic flow heat exchanger that transfers heat to and from the working fluid of the cryocooler; the displacer is either freely moving or driven by an external mechanism, driving the working fluid through the regenerator back and forth between the warm and the cold ends, and in Stirling and GM coolers the displacer is shaped as a piston whereas in the pulse-tube cooler a part of the fluid volume inside the tube acts as a freely moving displacer.

where T_h and T_c are the temperatures of the hot side and the cold side.

A pulse-tube cryocooler is not perfectly reversible due to the presence of the orifice, which has a flow resistance. It is crucial in this respect that in a pulse-tube cryocooler the work of expansion is not utilized [24]. The COP of an ideal pulse-tube cryocooler, $\eta_{\text{PT,ideal}}$, is given by [24]

$$\eta_{\text{PT,ideal}} = T_c/T_h. \tag{8}$$

A GM cycle includes isobaric cooling and warming processes, and isothermal compression and expansion processes. However, the mass-flow rates of the compression and expansion processes are not constant since there is flow into and out of the system through valves. The COP of an ideal GM cryocooler is given by [25,26]

$$\eta_{\text{GM,ideal}} = \frac{(p_h - p_l)V}{nRT_h\ln(p_h/p_l)}, \tag{9}$$

where p_h and p_l are the high intake pressure and the low exhaust pressure, respectively, V is the expansion volume, n is the number of moles flowing into and out of the cryocooler per cycle, and R is the universal gas constant.

The COP of the GM cryocooler approaches the ideal Carnot COP as the compression ratio falls to 1. That is because the entropy produced by the gas expansion through a valve reduces as the compression ratio decreases. However, in this case the available cooling power also drops to zero.

More details on the cooling principles of these fluid-based cryocoolers (recuperative as well as regenerative) can be found in the paper of De Waele [27] and the review of Radebaugh [21]. Theoretically, all these fluid-based cryocoolers can be scaled down to realize microcooling. In these fluid-based cryocoolers, compressors and check valves have moving parts at ambient temperatures, to drive and control the flows. From manufacturing perspective, there remain challenges in fabricating these moving parts in microscale. The scaling behavior of the fluid mechanics and the heat transfer involved in these cryocoolers is discussed in Sec. III. Available small-scale manufacturing technologies are considered in Sec. IV.

III. SCALING CONSIDERATIONS

Obviously there are limits to the scaling of cryocoolers to smaller and smaller sizes. Roughly, one can state that the gross cooling power scales with mass-flow rate [see Eq. (2)] and thus the volume of a cryocooler [see Eq. (15)] whereas parasitic heat loads due to conduction scales with size and due to radiation with area. Therefore, size reduction is limited by the fact that at some point the gross cooling power is no longer able to compensate for the parasitic heat loads, and the net cooling power becomes zero.

Furthermore, in microcooler systems it will be more difficult to maintain the required vacuum conditions. The outgassing rate scales with area and the gas permeation rate scales with area over wall thickness, whereas the vacuum space scales with volume. Therefore, the end-of-life vacuum pressure will be reached much faster in smaller systems.

Finally, the scaling of cryocoolers is limited by the manufacturing technologies that are available. In this section, the scaling with respect to cooling power and parasitics is considered as well as the scaling of the vacuum space. The manufacturing technologies are considered in Sec. IV.

In general, it is not easy to quantitatively estimate the difficulties that appear when cryocoolers are miniaturized. Nevertheless, it is worthwhile to present qualitatively the scaling effects with respect to cooling power and losses. In this section, the scaling effects of fluid-based cryocoolers are explained.

A. Recuperative cryocooler

1. Pressure drop and gross cooling power

The pressure drop in a recuperative cryocooler affects the cold-end temperature and the efficiency. The pressure drop of an internal fully developed flow in a channel with a length L can be calculated using the Darcy-Weisbach equation:

$$\Delta p = 0.5\rho v^2 f_D L/D_h, \tag{10}$$

where f_D is the Darcy friction factor, D_h is the hydraulic diameter, v is the mean flow velocity, which is determined by the mass-flow rate $\dot{m}$, the density ρ and the channel cross-section area A:

$$v = \frac{\dot{m}}{\rho A}. \tag{11}$$

For a fully developed laminar flow, the friction factor depends only on the Reynolds number, Re:

$$f_D = \frac{C}{\mathrm{Re}} = \frac{C\mu}{\rho v D_h}. \tag{12}$$

Here, C is a constant determined by the geometry and μ is the viscosity.

In this case, the pressure drop can be estimated by

$$\Delta p = 0.5\rho v^2 \frac{C\mu}{\rho v D_h} \frac{L}{D_h} = \frac{C\mu\dot{m}L}{2\rho A_h^2} \propto \frac{\dot{m}}{x^3}. \tag{13}$$

where x represents the size of the cryocooler and the vacuum chamber discussed in subsection C.

It is important here to note that all dimensions are assumed to scale with the same factor. The pressure drop increases with decreasing size for a given mass-flow rate. A higher pressure drop along the low-pressure channel of a JT cryocooler results in a higher boiling temperature in the evaporator and thus in a higher cold-end temperature. In this scaling analysis we assume the pressure drop is kept constant. Then, according to Eq. (13), the mass-flow rate scales with the cube of the size:

$$\dot{m} \propto x^3. \tag{14}$$

Since the gross cooling power is proportional to the mass-flow rate [see Eqs. (2)–(4)], in scaling, it also is proportional to the cube of the size:

$$\dot{Q}_c \propto \dot{m} \propto x^3. \tag{15}$$

2. Conduction loss

Due to the large temperature gradient in the material of the CFHX, the thermal conductivity loss through the CFHX is a significant loss, given by

$$\dot{Q}_{\mathrm{cond}} = \lambda_{\mathrm{eff}} A dT/dx \propto x, \tag{16}$$

where λ_{eff} is the effective conductivity of the material of the CFHX, A is the cross-section surface area of the CFHX, and dT/dx is the temperature gradient along the CFHX.

3. Radiation loss

The heat transfer through radiation takes place through electromagnetic waves mainly in the infrared region. Two entities at different temperatures can exchange heat through radiation. When the surface of the vacuum chamber is much larger than the surface of the cryocooler, the radiative heat transfer is represented by

$$\dot{Q}_{\mathrm{rad}} = \epsilon\sigma_B A_{\mathrm{cooler}}\left(T_{\mathrm{amb}}^4 - T_c^4\right) \propto A_{\mathrm{cooler}} \propto x^2, \tag{17}$$

where σ_B is the Stefan-Boltzmann constant, ϵ is the emissivity of the cryocooler, T_{amb} and T_c are the ambient and cryocooler temperatures, and A_{cooler} is the outside surface of the cryocooler.

4. Heat-exchange loss

In optimizing the design of a CFHX, it is useful to express losses (thermal and viscous) in terms of the entropy that is produced due to these losses as $\dot{Q}_{\mathrm{loss}} = T\Delta\dot{S}_{\mathrm{prod}}$ [28,29]. The entropy $\dot{S}_{\mathrm{prod}}$ generated in the heat exchange between high-pressure gas, heat-exchanger material, and low-pressure gas can be expressed by their temperature profiles along the heat exchanger, represented by T_h, T_m, and T_l:

$$\frac{d\dot{S}_{\mathrm{prod},hx}}{dl} = \frac{t_{\mathrm{eff},h}}{2\lambda_m} \frac{(\dot{m}c_p)^2}{OT_hT_m}\left(\frac{dT_h}{dl}\right)^2 + \frac{t_{\mathrm{eff},l}}{2\lambda_m} \frac{(\dot{m}c_p)^2}{OT_lT_m}\left(\frac{dT_l}{dl}\right)^2, \tag{18}$$

where λ_m is the heat-conduction coefficient of the CFHX material, O is the channel perimeter, and $t_{\mathrm{eff},h}$ and $t_{\mathrm{eff},l}$ are effective thicknesses of the high- and low-pressure channel, respectively [28]:

$$t_{\mathrm{eff},h} = t + \frac{2\lambda_m}{h_h} = t + 2\lambda_m\left(\frac{D_h}{\lambda_g\mathrm{Nu}}\right)_h \propto x, \tag{19}$$

$$t_{\mathrm{eff},l} = t + \frac{2\lambda_m}{h_l} = t + 2\lambda_m\left(\frac{D_h}{\lambda_g\mathrm{Nu}}\right)_l \propto x, \tag{20}$$

where h is the convective heat-transfer coefficient, D_h is the dydraulic diameter, t is the thickness of the wall, and Nu is the Nusselt number.

Combining Eqs. (14) and (18)–(20) gives

$$\frac{\dot{S}_{\mathrm{prod},hx}}{dl} \propto \frac{\dot{m}^2}{x^2} \propto x^4. \tag{21}$$

Therefore, the power lost due to the imperfect heat exchanger in the CFHX scales with x^5.

$$\dot{Q}_{hx} = d\dot{S}_{\mathrm{prod},hx} \propto x^5. \tag{22}$$

Since the heat-exchange losses scale with x^5 whereas the cooling power scales with x^3, it is clear that these heat-exchange losses will not limit the scaling to smaller size, but rather may limit upscaling to larger size.

5. Viscous loss

In laminar flows (which is the case for small channels) the entropy produced in a section of the channel can be expressed as [28]

$$\dot{S}_{\text{prod},fr} = \frac{\dot{m}}{\rho T} \frac{C}{2} \frac{\mu v}{D_h^2} dl. \tag{23}$$

Using Eq. (23) we can write

$$\frac{\dot{S}_{\text{prod},fr}}{dl} = \frac{\dot{m}^2}{\rho^2 AT} \frac{C}{2} \frac{\mu}{D_h^2} \propto \frac{\dot{m}^2}{x^4} \propto x^2. \tag{24}$$

Therefore, the power losses due to the flow resistance in CFHX is

$$\dot{Q}_{fr} = T\dot{S}_{\text{prod},fr} \propto x^3. \tag{25}$$

6. Expander loss

Here, expanders refer to any mechanical device that converts the fluid exergy to work. Ideally, the fluid undergoes isentropic expansion process through the expander. In the real case, various irreversibilities increase the entropy of the fluid, which results in less shaft work than the ideal isentropic work. The increase in entropy occurs due to the viscous friction in either boundary layers, free shear layers, heat transfer across finite-temperature differences, and nonequilibrium processes in very rapid expansions or in shock waves [30]. These entropy-production terms are determined not only by the turbine size but also by the turbine type and configuration. Moody developed an empirical correlation of the turbine efficiency (η, the ratio of work delivered by the actual turbine to work delivered by an isentropic turbine) as a function of the turbine

diameter D [31]:

$$\frac{1-\eta_2}{1-\eta_1} = \left(\frac{D_1}{D_2}\right)^{0.25}. \tag{26}$$

From Eqs. (15) and (26), we can find that larger turbines are more efficient, and the expander loss is

$$\dot{Q}_{\text{exp}} \propto \dot{m}(1-\eta) \propto x^{2.75}. \tag{27}$$

7. Total losses

Figure 4 summarizes qualitatively the scaling effect on various parasitic loss due to heat exchange, conduction, radiation, flow resistance, and expander in a recuperative cryocooler. As can be seen from the figure, the conduction is the dominant loss term at small size.

8. Measures to increase the net cooling power

In order to increase the net cooling power of a recuperative microcooler with a given size, we could either increase the gross cooling power or decrease the parasitic losses.

The gross cooling power of a recuperative cryocooler increases with increasing mass-flow rate and with increasing specific enthalpy difference of the gas between the outlet and the inlet of the cryocooler. At fixed size the mass-flow rate can only be increased by increasing the pressure difference produced by the compressors, resulting in a higher pressure drop along the cryocooler. At fixed size and fixed pressure drop, the only thing we can do is to increase the specific enthalpy difference—for instance, increasing the charge pressure, replacing the pure gas by a mixture [32], or by using precooling [33].

The other option is reducing the parasitic losses that include conduction loss, radiation loss, viscous loss, expander loss, and heat-exchange loss.

Conduction loss is proportional to the material conductivity; therefore, materials with low conductivities are
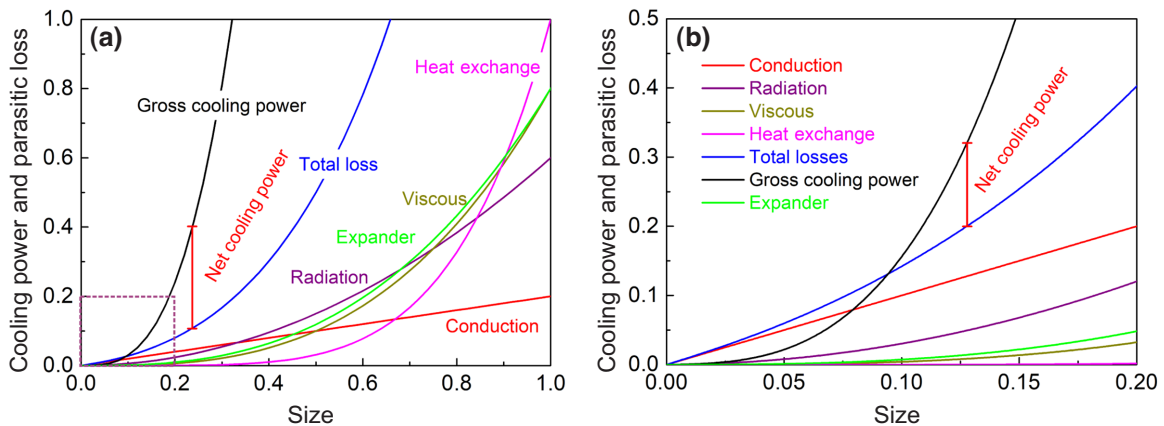

FIG. 4. (a) Parasitic losses of recuperative cryocoolers versus size; (b) enlargement of the rectangular area near the origin shown in (a). Units for all plotted quantities are arbitrary.
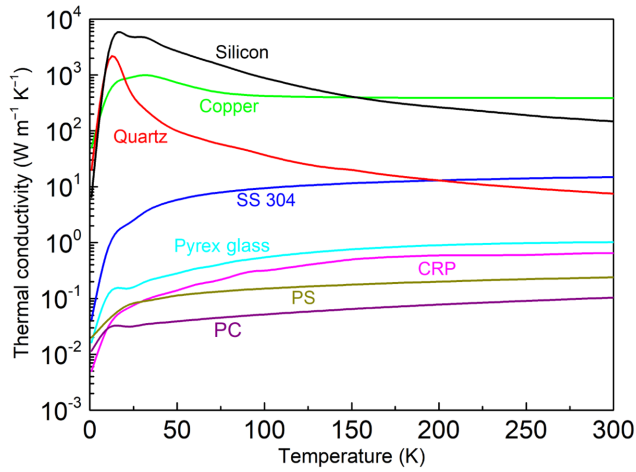
FIG. 5. Temperature dependence of the thermal conductivity of several materials from Cryocomp [34] and MPDB [35]. CRP, carbon-reinforced plastic; SS 304, stainless steel 304; PS, polystyrene; PC, polycarbonate.

preferred. Figure 5 gives the conductivity of different materials, in which Pyrex glass, carbon-reinforced plastic, polystyrene, and polycarbonate have much lower thermal conductivity than materials like silicon and copper. As indicated above, conduction is the dominating loss in scaling to small size. A further way to reduce conduction loss is increasing the ratio of the cross-section surface area to the length of the cryocooler design [see Eq. (16)].

Radiation loss is proportional to the emissivity of the cryocooler surface when the surface of the surroundings is much larger than that of the cryocooler. When the cryocooler is made of a material with a high emissivity, for instance, glass with emissivity of 0.8–0.95 [36], it can be covered with a thin layer of material with low emissivity (for instance, gold with emissivity of 0.02 [37]). Viscous loss is proportional to the friction factor, and decreasing the friction factor can be realized by optimizing the inner structure and the geometry of the flow channel [38–40]. Heat-exchange losses reduce with increasing Nusselt number [see Eqs. (18)–(20)], and a higher Nusselt number can be realized by optimizing the inner structure of the flow channel [40].

B. Regenerative cryocooler

1. Gross cooling power

The gross cooling power $\dot{Q}_c$, of a regenerative cryocooler is given by [41]

$$\dot{Q}_c = \pi f V_{\text{gas}} p_0 \left(\frac{p_1}{p_0} \right) \cos \theta \propto f \times V_{\text{gas}} \times p_1 \propto x^3, \quad (28)$$

where f is the frequency, V_{gas} is the gas volume amplitude, p_0 is the average pressure, p_1 is the amplitude of the

sinusoidal pressure, and θ is the phase angle by which the volume flow $\dot{V}$ leads the sinusoidal pressure p.

The volume flow and the sinusoidal pressure are given by

$$\dot{V} = 2\pi f V_{\text{gas}} \cos(\omega t + \theta) \quad (29)$$

and

$$p = p_0 + p_1 \cos \omega t, \quad (30)$$

where ω is the angular frequency.

2. Parasitic losses

Losses in regenerative cryocoolers due to conduction and radiation scale similar as in recuperative cryocoolers. These losses are expressed by Eqs. (16) and (17). As indicated before, the losses due to heat exchange will not limit the miniaturization and are not considered here. Apart from conduction and radiation, viscous losses may play a role. The pressure in a regenerative cryocooler varies harmonically in time as expressed in Eq. (30) with a phase difference between compressor and cold stage. As a result, gas flows from compressor to cold tip and back. Viscous losses mainly occur in the flow through the regenerator. The associated pressure drop varies also harmonically with the same frequency; $\Delta p = \alpha p_1 \sin(\omega t + \varphi)$. Here φ is representing the phase angle and α represents the ratio between the pressure-drop amplitude and the gas-pressure amplitude. In well-designed regenerators this ratio is around 15%.

The resulting viscous losses can thus be expressed as

$$\dot{Q}_{\text{visc}} \propto f \times \Delta p \times V_{\text{gas}} \propto f \times p_1 \times V_{\text{gas}} \propto x^3. \quad (31)$$

According to Eqs. (28) and (31), both the gross cooling power and parasitic loss due to flow resistance of a regenerative cryocooler are proportional to the cube of its size as was the case in recuperative cryocoolers. As stated above, radiation and conduction losses also scale in the same way as in a recuperative cryocooler. Therefore, the scaling effects on the cooling power and various parasitic losses in a regenerative cryocooler are similar to the cases in a recuperative cryocooler, and the conduction is the dominant loss term at small size (see Fig. 4).

3. Measures to increase the net cooling power

The conduction and radiation losses of a regenerative cryocooler can be reduced in a similar way as in a recuperative cryocooler. The gross cooling power of a regenerative cryocooler is the product of the frequency, the pressure amplitude and/or the volume of the gas channel. To increase the gross cooling power of a regenerative cryocooler with a given size, we could increase the absolute
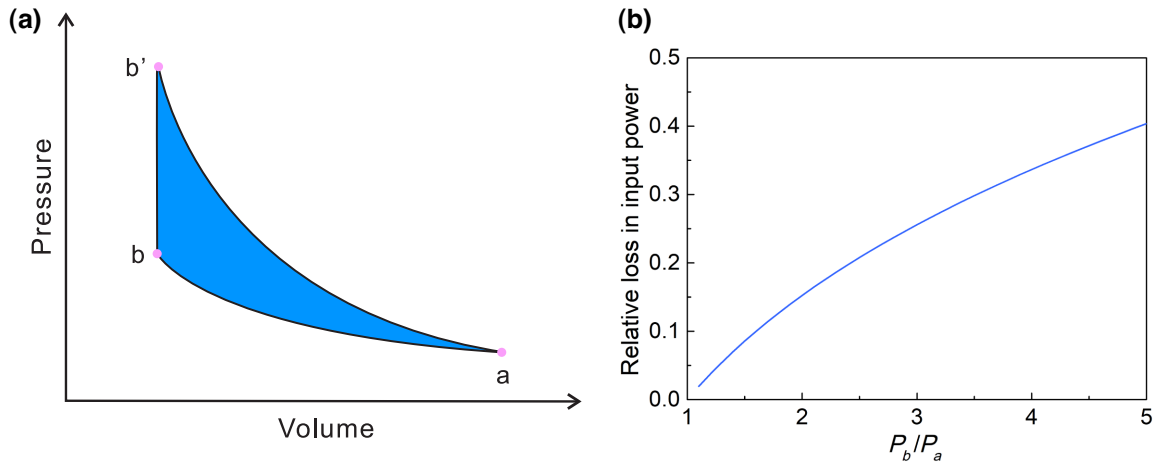
FIG. 6. (a) Adiabatic compression ($a \rightarrow b'$) compared to isothermal compression ($a \rightarrow b$). The blue area represents the extra work that is required for adiabatic compression of the gas from volume V_a to volume V_b. (b) Relative loss as a function of pressure ratio.

pressure amplitude or the frequency. In small cryocoolers very high filling pressures are possible but achieving high-pressure amplitudes, certainly at higher frequencies, will be challenging. Increasing the operating frequency, apart from possibly reducing the pressure amplitude, will increase viscous losses. Furthermore, the thermal loss of the compressor also increases with increasing frequency. That is because the compression will be more and more adiabatic instead of isothermal as the frequency increases. This is discussed in more detail below.

In an adiabatic compression of an ideal gas [$a \rightarrow b'$, see Fig. 6(a)], the work done to the system is equal to

$$W_{\mathrm{adi}} = \frac{\gamma}{\gamma - 1} nRT_a \left[\left(\frac{p_{b'}}{p_a} \right)^{(\gamma-1)/\gamma} - 1 \right], \qquad (32)$$

where γ is the ratio of the specific heats c_p/c_v, which is 5/3 for helium.

For an isothermal process [$a \rightarrow b$, see Fig. 6(a)], the reversible work involved when an ideal gas is compressed from state a to state b is equal to

$$W_{\mathrm{iso}} = nRT_a \ln \left(\frac{p_b}{p_a} \right). \qquad (33)$$

Compared to the isothermal process, the extra power (the blue area shown in Fig. 6) done to the system through the adiabatic process is

$$W_{\mathrm{lost}} = W_{\mathrm{adi}} - W_{\mathrm{iso}}. \qquad (34)$$

The relative extra power $W_{\mathrm{lost}}/W_{\mathrm{iso}}$ for helium gas increases with the pressure ratio, as shown in the right plot of Fig. 6.

C. Vacuum

Microcoolers require vacuum insulation to minimize the parasitic loss that is due to the heat flow from the warm environment via the surrounding gas. As shown in Fig. 7, the heat load on the microcooler from the environment includes conduction and radiation. In the free molecular flow regime, the conductive heat load increases with increasing surrounding pressure. Usually the design of the microcooler package aims to have the conductive heat load due to residual gas in the vacuum to be less than the radiative heat load. The pressure corresponding to that transition is about 0.01 Pa. Since both the radiation and gas conduction are proportional to the surface area of the microcooler, scaling has no effect on the pressure at that transition point.

The increase in the pressure of a vacuum chamber is due to the gases and vapors that are released from the chamber surface by means of various mechanisms including internal and real leaks, vaporization, desorption, diffusion, and permeation [43]. Internal leaks such as gas pockets and
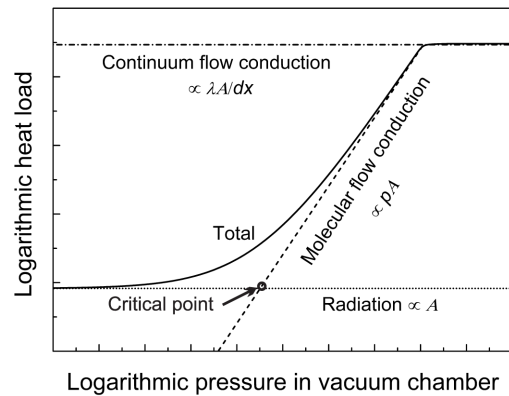

FIG. 7. Heat load on a microcooler versus pressure in a vacuum chamber (adapted from Ref. [42]).

real leaks caused by pathways through physical damages should and can be prevented by proper design and careful manufacturing. Vaporization can be prevented by proper material section. The remaining two causes of pressure increase, desorption, and permeation, cannot be prevented but can be reduced and are considered here [42].

Desorption is the release of adsorbed adsorbates from the surface of the adsorbent. These adsorbates can result from direct adsorption or from the final step in a permeation process. Desorption of water adsorbed on the internal surfaces of a vacuum chamber often affects the life time of the vacuum chamber.

The desorption rate, $\dot{N}_{\text{des}}$ (Pa m^3 m^{-2} s^{-1}), can be expressed as a first-order reaction:

$$\dot{N}_{\text{des}} = \frac{N}{\tau_0} \exp\left(-\frac{E}{RT}\right), \qquad (35)$$

where N is the surface density of molecules, τ_0 is the nominal period of vibration of the bond between the adsorbed molecule and the substrate, which is usually taken to be about 10^{-13} s, R is the universal gas constant, T is the temperature, and E is the activation energy of desorption.

The increase in pressure due to the desorption is given by

$$\frac{dp}{dt} = \dot{N}_{\text{des}} \frac{A}{V} k_B T \propto x^{-1}. \qquad (36)$$

Permeation is a three-stage process, consisting of the adsorption of gases at the exterior surface of the wall, the diffusion through the wall, and the desorption at the interior surface. The permeation of helium or hydrogen existing in environments usually affects the life time of a vacuum chamber.

In general, the diffusion through the wall determines the permeation rate, $\dot{N}_{\text{per}}$ (Pa m^3 m^{-2} s^{-1}), which is described by

$$\dot{N}_{\text{per}} = \frac{DSp^n}{d}, \qquad (37)$$

where D is the diffusivity, S is the solubility, p is the partial pressure of the gas under consideration, n is a constant that is dependent on the gas and the material of the chamber wall, and d is the wall thickness.

The increase in pressure due to the permeation is given by

$$\frac{dp}{dt} = \dot{N}_{\text{per}} \frac{A}{V} k_B T \propto x^{-2}. \qquad (38)$$

These Eqs. (36) and (38) indicate that a smaller size will cause a faster pressure increase and thus a shorter "vacuum life." Imagine as an example a cryocooler system of which the size is of the order of 1 meter and this system has a vacuum life time of 10 years. And assume we scale down that system to centimeter size using the same materials and vacuum techniques. Then, the vacuum life time of that down-scaled system would be of the order of 1 month, or even less if permeation contributes significantly to the gas-pressure increase. As indicated above vacuum is a challenge in small-scaled cryosystems. Careful manufacturing along with additional sorbents installed in the vacuum space are required for establishing operating times of multiple years [42].

IV. MICROSCALE MANUFACTURING TECHNOLOGIES

In order to meet the demands of miniaturization trends, various microscale manufacturing technologies-manufacturing processes for creating miniature devices or components with dimensions that are in the range of a few tens of nanometers to a few millimeters [44], have been developed to have better quality devices, and cheaper and more effective processes. In this section, a review is given of these microscale manufacturing technologies split in lithographic and nonlithographic technologies. Lithographic micromachining technologies are derived from the microelectronic processes that include patterning, etching (like chemical etching and powder blasting), bonding, and dicing. Nonlithographic micromachining technologies are either miniaturized versions of macroscale processing techniques or techniques newly conceived for microscale manufacturing such as mechanical micromachining (MMM), electrical-discharge machining (EDM), and additive manufacturing (AM), also known as 3D printing. Table II gives a comparison of these micromachining technologies.

TABLE II. Comparison of micromachining technologies.

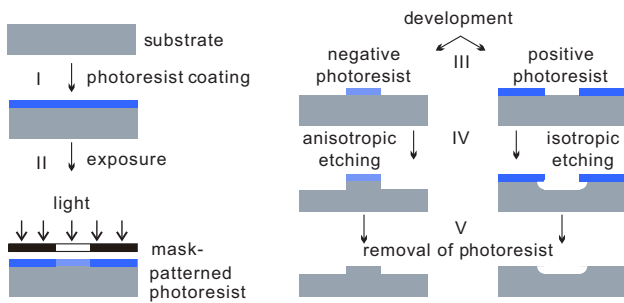| Machining method	Minimum feature	Tolerance	Production rates	Materials
Chemical etching [45]	13 nm	1 nm	Method-dependent	Silicon, glass
Powder blasting [46]	50 μm	2.5 μm	High	Brittle materials
MMM [47]	10 μm	1 μm	High	Any
EDM [47]	10 μm	1 μm	High	Conductive materials
AM [48]	2 μm	25–100 nm	Feedstock-dependent	Plastic, metal, ceramics and glass

FIG. 8. Main processing steps of the photolithography (adapted from Ref. [50]).

A. Lithographic micromachining technologies

Lithographic micromachining technologies include patterning, etching (chemical and physical), bonding, and dicing [49].

1. Patterning

Lithography involves formation of patterns on a photoresist, which is deposited on a substrate. In this process, the substrate is first coated with a thin photoresist layer. The substrate is then exposed to radiation of a particular wave length through a mask (a transparent photomask coated with an opaque pattern), causing either weakening of positive photoresist or strengthening of negative photoresist. The weaker photresist is removed by applying a solvent (developer) to the surface. Thus the mask is copied positively or negatively onto the substrate (see Fig. 8).

2. Chemical etching

In the etching process, the material of the wafer is removed selectively using the patterned photoresist as a mask. There are two basic categories of etching processes: chemical etching and powder blasting. Chemical etching includes wet etching and dry etching. In wet etching, the material of the wafer is dissolved by immersing it in a chemical solution. Whether the etching is isotropic or anisotropic depends on the properties of the wafer material

and the solution. In dry etching, the material of the wafer is sputtered or dissolved using ions or plasma (mixture of electrons, ions and neutrals). Plasma etching refers to the process that is purely chemical, whereas reactive ion etching (RIE) refers to the process in which ion bombardment of the wafer surface plays a synergistic role in the chemical reaction [51]. Deep reactive-ion etching (DRIE) is a highly anisotropic etching process used to create structures with high aspect ratios.

3. Powder blasting

In powder blasting a high-velocity air jet containing powder particles is used to impinge on and erode material from a surface [46,53,54]. When a powder particle indents the surface of a brittle material such as glass or silicon it generates cracks and a plastic zone around the impact point. Powder blasting is a pure mechanical process, and the mask material for powder blasting is required to be ductile and thick, in order to prevent the particles penetrating through the mask and damage the work piece. Powder blasting is, because of its high aspect ratio and relatively large minimum feature, mainly used for creating small holes and slits through a wafer.

Figure 9 shows the differences of typical products fabricated by using isotropic chemical etching, anisotropic reactive ion etching, and powder blasting. Compared to chemical etching, powder blasting results in a higher surface roughness.

4. Wafer bonding

In order to create a closed volume in a channel as part of a microcooler, two wafers need to be stacked, one containing the volume or channel and the other closing it. The two wafers need to be firmly connected. Such a fixation of wafers can be established by bonding [49]. This section discusses fusion and anodic bonding that are the most commonly used technologies in microfluidics.

Fusion bonding refers to the process of adhesion of two highly polished wafers without using any intermediate gluing layers (see Fig. 10). In fusion bonding, the wafers are
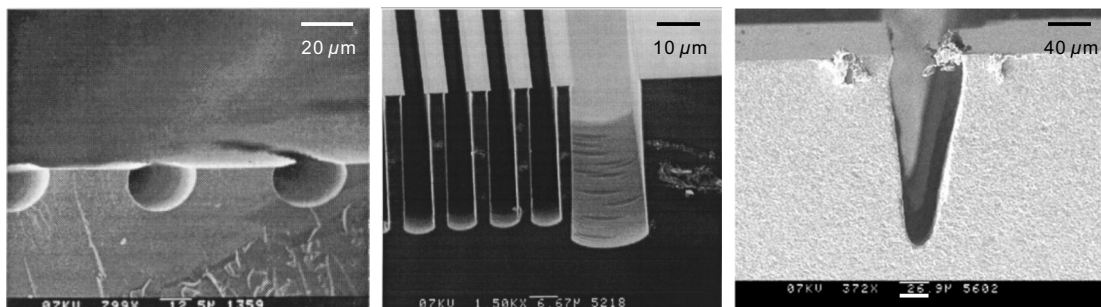

FIG. 9. Typical products of isotropic chemical etching, anisotropic reactive ion etching, and powder blasting (adapted from Ref. [46,52]).

(a) Silicon wafer

1000 °C

Fusion bonding (silicon-silicon)

(b) Glass wafer

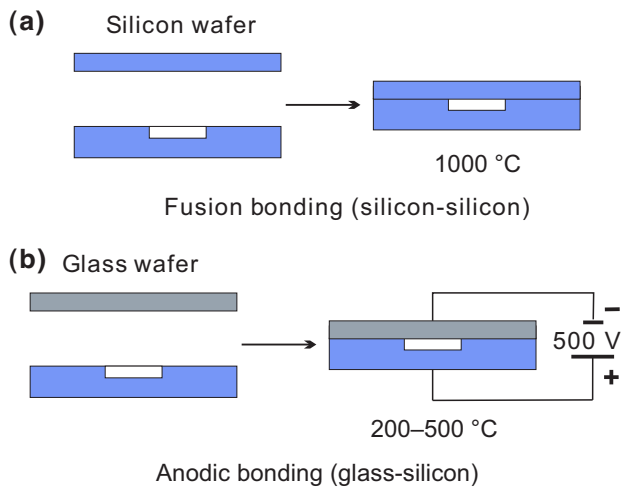
500 V

200–500 °C

Anodic bonding (glass-silicon)

FIG. 10.   Schematic of the fusion bonding and anodic bonding.

firstly prebonded at room temperatures via relatively weak intermolecular attractive forces, such as van der Waals forces or forces associated with hydrogen bridge bonds. Subsequent annealing at elevated temperatures of about 1000 °C results in much higher bond strengths via covalent bonds [55]. The bonding includes three procedural steps, namely, wafer preprocessing, prebonding at room temperatures, and annealing at elevated temperatures.

Anodic bonding is a wafer-bonding process to seal glass to either silicon or metal without introducing an intermediate layer (see Fig. 10); it is commonly used to seal glass to silicon wafers in electronics and microfluidics. During the anodic bonding, wafers are heated up to about 200–500°C, and then a dc voltage of about 500 V is applied across the wafers (see Fig. 10). The electrical field causes the positively charged ions (sodium ions in glass) to migrate through the glass to the negative electrode, leaving the stronger bound negative ions behind. After the positive ions have drifted towards the cathode, a large potential drop occurs at the glass-silicon interface, which pulls the wafers together. Here the silicon and oxygen react, forming a SiO_2 layer, which gives the strong bond between silicon and glass.

5. Dicing process

During the dicing process, the bonded substrates are divided into single units, or dices. The dicing process is accomplished by mechanically sawing or laser cutting the bonded substrate in areas between the units (often referred to as either dicing streets or scribe lines).

B. Nonlithographic micromachining technologies

As mentioned above, the nonlithographic technologies are mechanical micromachining, electrical discharge machining and additive manufacturing. These are discussed in more detail below.

1. Mechanical micromachining

Mechanical micromachining, scaled-down versions of traditional material removal processes as turning, milling, and drilling, is closest to traditional tool technology [57]. A specific technology to be mentioned is laser-beam micromachining and laser-beam welding [58,59]. It has advantages in terms of material choices and complexity of produced geometry. Figure 11 shows some mechanical micromachined cryocooler components.

2. Electrical-discharge machining

Electrical-discharge machining is the process of machining electrically conductive materials by using precisely controlled sparks that occur between an electrode and a component in the presence of a dielectric fluid [see Fig. 12(a)] [60,61]. The spark vaporizes the surface of the component, shaping it in the desired manner. EDM is primarily used for hard metals or those that would be very difficult to machine with traditional techniques, for instance, laser sintered metal parts made by 3D printing. Figure 12(b) shows the image of a microhole with a diameter of about 115 μm obtained by EDM.

3. Additive manufacturing

Additive manufacturing (AM), differing from the conventional method based on removing material, can build complex components by adding layer upon layer of material such as plastic, metal, ceramics, and glass. Minimum feature size in AM is generally limited by the feedstock state such as powder, wire, sheet, and ink. Various overviews of additive manufacturing techniques have been given in the literature [63–66].

A specific AM method that has been used to fabricate miniature components of cryogenic systems is selective laser sintering (SLS). This method uses a laser to sinter powder of plastic, ceramic, glass, metal, or other materials to build an object [see Fig. 13(a)]. The SLS process sinters the powders layer by layer. After one layer is built, the powder feed tray raises, a roller transfers new powder to the build tray as needed, and another layer is built on top of the existing layers. This process is repeated until the object is complete. Vanapalli *et al.* developed a compact flat-panel heat switch with a gas-gap spacing of 200 μm operating at room temperature [67] and cryogenic temperatures [68]. The heat switch is produced from Ti-6Al-4V powder by using a selective laser-sintering method [see Fig. 13(b)]

Other examples of additively manufactured cryocooler components are depicted in Fig. 14. Figure 14(a) shows a 3D-printed support of the third stage a 4 K cryocooler developed by University of Glasgow and Rutherford Appleton Laboratory. The support is made of VeroGrey giving structural stability with a low thermal conductance [69]. Figure 14(b) shows a 3D-printed supporting structure
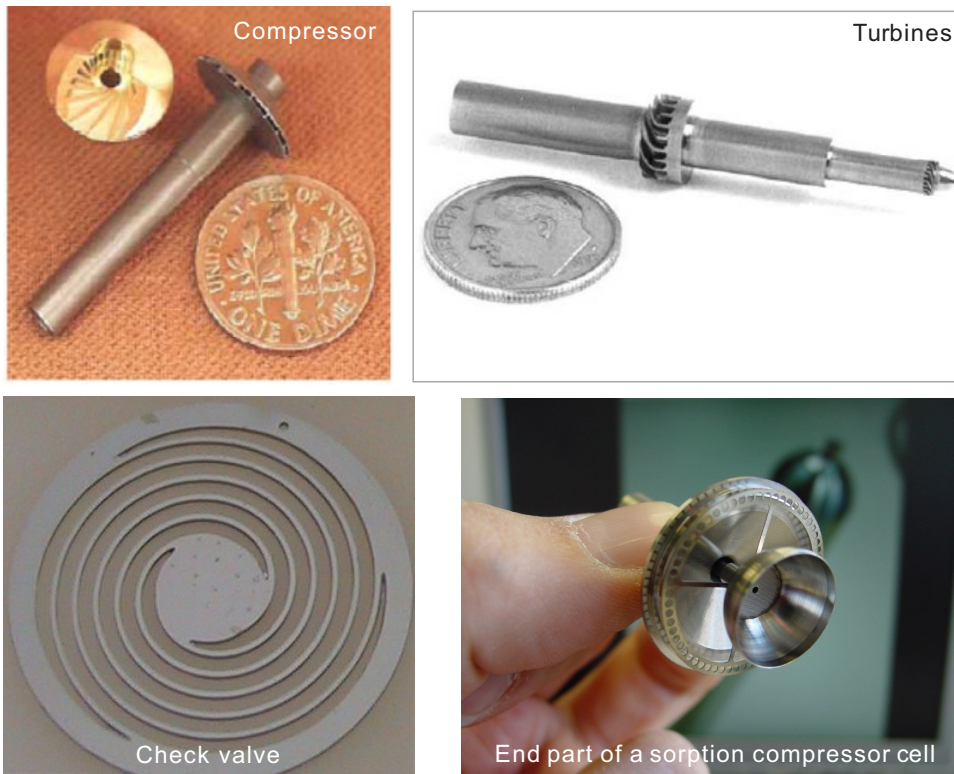
FIG. 11. Mechanical micromachined cryocooler components. The top two photos show compressor and expander turbines developed by Creare [56], and the bottom photos are from University of Twente and show the flap of a passive valve outer diameter of 11 mm and the end part of a sorption compressor cell.

made of Ti-6Al-4V. The support thermally insolates the 300 K outside from the 103 K intermediate stage. Inside the 103 K enclosure an IR detector is cooled to 40 K [70,71].

V. PROGRESS IN THE MINIATURIZATION OF CRYOCOOLERS

This section reviews developments in miniaturization of both recuperative and regenerative cryocoolers.

A. Developments on recuperative microcoolers

Since the 1980s, there have been several studies on the miniaturization of JT cryocoolers, dealing with the

optimization of the CFHX and with various techniques for manufacturing the cold stage [28,72–78]. In this section, the development of JT microcoolers is reviewed.

1. Stanford University and MMR Technologies, Inc.

Little *et al.* pioneered the work on recuperative microcoolers by using lithography-based micromachining technologies. They made the first microcooler by using silicon and glass [79], which was successfully used to operate with CO_2 and ethylene. However, the microcooler did not work with N_2 because of the thermal losses caused by the large thermal conductivity of silicon.
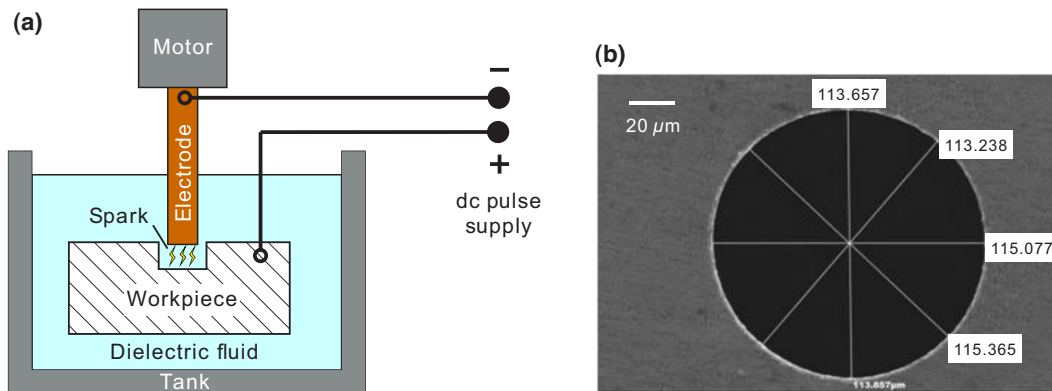

FIG. 12. (a) Schematic of electric discharge machining; (b) SEM image of a microhole obtained by micro EDM in NiTi shape memory alloy (adapted from Ref. [62]).
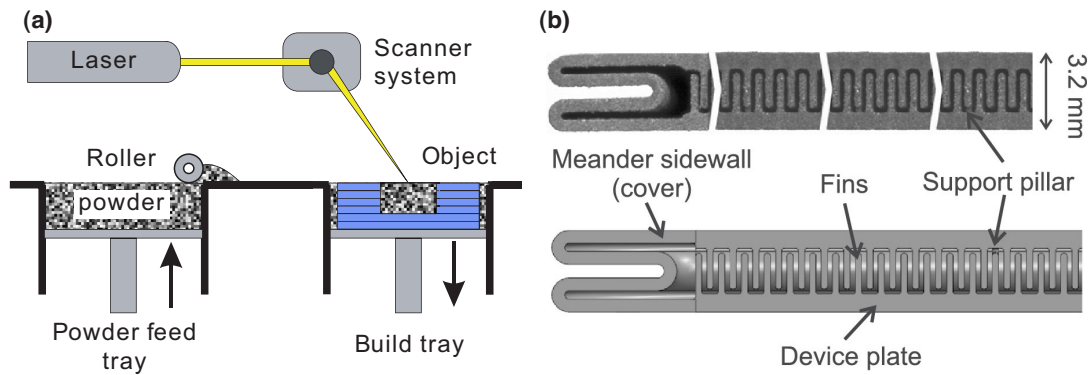
FIG. 13.   (a) Principle of SLS method; (b) Heat switch produced by SLS (adapted from Ref. [67]).

Garvey *et al.* [73] developed a microcooler with a size of $0.5 \times 2 \times 15$ mm [see Fig. 15(a)]. The microcooler was made of glass wafers by using an abrasive etching process. The microcooler operated with nitrogen gas and produced a cooling power of 25 mW at 88 K. To further reduce the cold-end temperature, a design with serial two-stage expansion of Linde [80] was adopted to reduce the pressure drop along the low-pressure channel. In the design with serial two-stage expansion of Little, 80% of the gas first expanded to 2.6 MPa, while the remaining 20% expanded further to 0.11 MPa [81]. This design resulted in a smaller mass-flow rate through the evaporator, allowing a lower pressure and consequently a lower temperature of 80 K. The internal structure of the microcooler is given in Ref. [81].

To realize the cooling of infrared detectors with an operation temperature below 80 K. Little *et al.* developed a fast cool-down microcooler with a size of $1.25 \times 12.5 \times 45$ mm [see Fig. 15(b)]. It consisted of five glass substrates each of 0.025 cm thickness and its internal structure is given in Ref. [82]. The high-pressure channel of the microcooler is a serpentine channel with a width of 86 μm and a height of 40 μm, while the low-pressure channels have deeper and wider channels (no specific values were given). The microcooler had two stages that were operated with nitrogen-hydrocarbon gas mixtures (28.8% N_2, 39.5% CH_4, 27.7% C_2H_6, and 4% C_3H_8) and nitrogen, respectively. The reason for using two stages is to realize fast cooldown because the stage of the nitrogen-hydrocarbon gas mixtures provided large refrigeration capacity to obtain a rapid cooldown of the bulk of the microcooler and to precool the nitrogen stage and increase the efficiency of that stage. By pumping on the nitrogen exhaust with an external vacuum pump, the microcooler cooled down from 300 K to 70 K in 14 s.

A disadvantage of the JT expansion is that cooling only occurs if the initial temperature of the gas, prior to expansion, is below the inversion temperature of the gas.
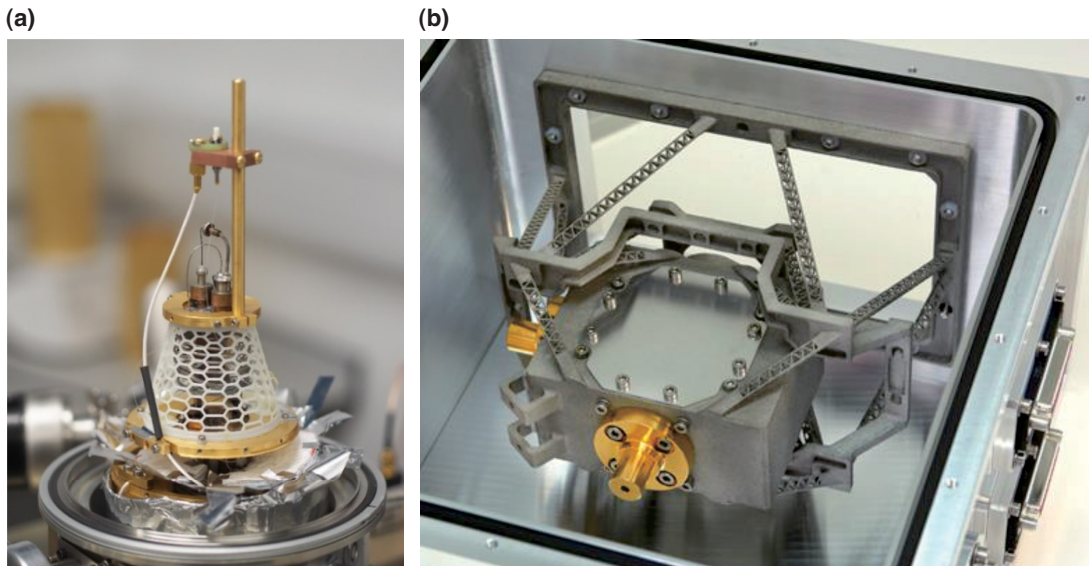

FIG. 14.   (a) 3D-printed thermal isolation mount made of VeroGrey (adapted from Ref. [69]). (b) Monolithic support structure made of Ti6Al4V (adapted from Ref. [71]).
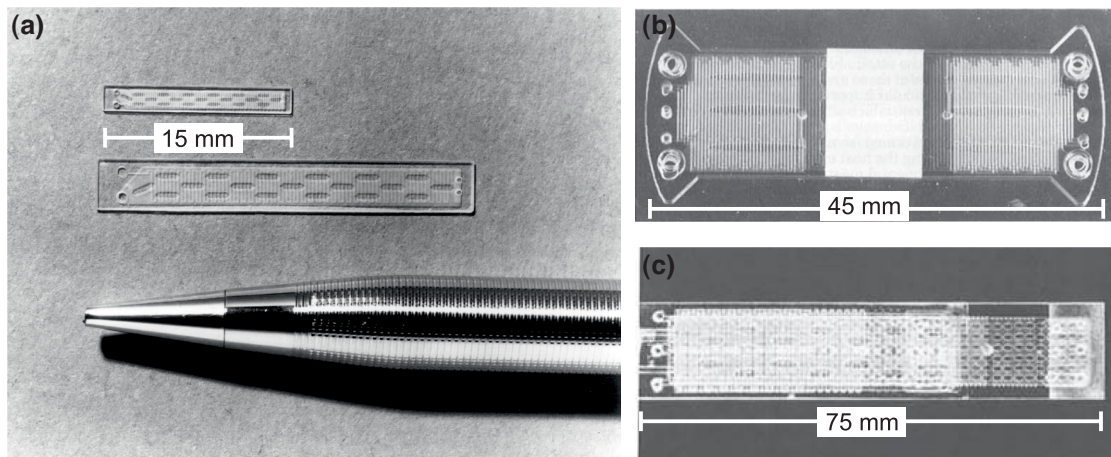
FIG. 15.   Microcoolers developed at Stanford University and MMR. (a) 88 K single-stage nitrogen JT cryocooler (adapted from Ref. [10]); (b) 77 K two-stage nitrogen-hydrocarbon gas mixture-nitrogen JT cryocooler (adapted from Ref. [83]); (c) 20 K two-stage nitrogen-hydrogen JT cryocooler (adapted from Ref. [84]).

In order to reach temperatures near the normal boiling points of neon, hydrogen, or helium in a JT cryocooler starting from ambient temperature, a multistage JT cryocooler is required. Little reported a seven-wafer stack two-stage microcooler with a total length of 75 mm [84] [see Fig. 15(c)]. The two-stage microcooler using nitrogen and hydrogen as working fluids was designed for operating at around 20 K region, however, the measured performance of the two-stage microcooler was not reported. The measured performance of an 85-mm-long two-stage microcooler operated with nitrogen and neon was reported [85]. The nitrogen stage had a cold-end temperature of 89 K and the neon stage had a cooling power of 100 mW at 34 K.

Besides the 70 K and 80 K microcoolers, the internal structure and dimensions of Little's other designs were not described in detail. Little patented several designs of microcoolers with different internal structures [86], however, the patented designs are different from the adopted design. For instance, the patented design of the two-stage microcooler is composed of five wafers, whereas the adopted design consists of seven wafer layers.

2. University of Twente

At the University of Twente, ter Brake *et al*. started the research on microcooling in the late 1990s [87,88]. The development of microcoolers includes the development in fabrication technology and thermodynamic modeling [89]. Fabrication technology went through three stages, namely, handmade, semimicromachined, and fully micromachined (see Fig. 16).

Holland *et al*. presented two handmade cryocoolers with glass-tube heat exchangers [76] (see Fig. 16). In both cryocoolers a tube-in-tube CFHX was used, one with a length of 270 mm, the other 105 mm. The tubes were made of fused silica glass with inner and outer diameters of 0.1 and 0.36 mm, and 0.53 and 0.67 mm, respectively. The restrictions of the cryocoolers could be tuned at the room-temperature side of the cryocooler. Operated with nitrogen gas between 0.1 and 10.0 MPa, a minimum temperature of 82 K could be obtained by both cryocoolers with different mass-flow rates.

Burger *et al*. explored the possibility to fabricate JT cryocooler parts by means of micromachining technology [11,90] (see Fig. 16). They realized a semimicromachined
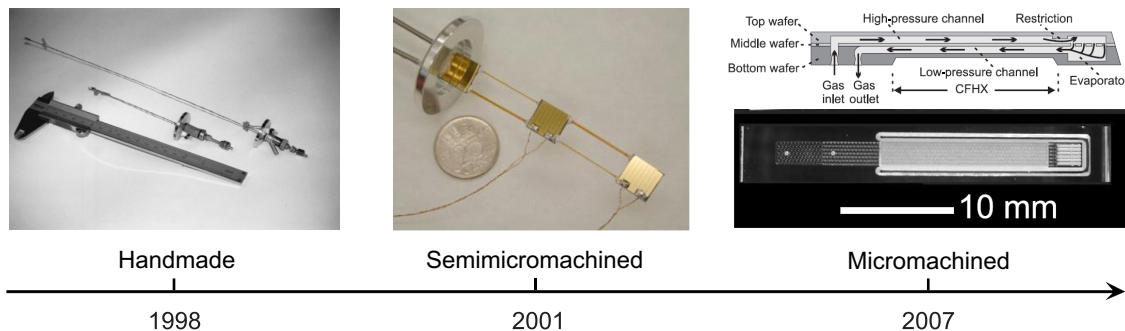

FIG. 16.   Development line in fabrication technology of microcoolers at University of Twente (adapted from Refs. [76,78,90]).
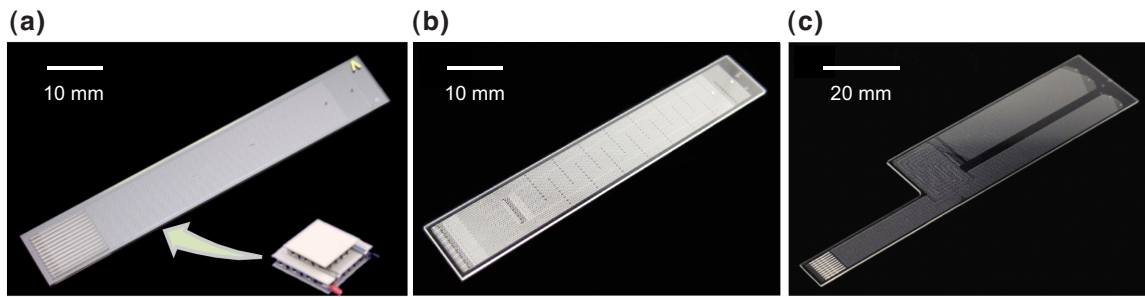
FIG. 17.   Micromachined cryocoolers developed at university of Twente (adapted from Ref. [89]). (a) 100 K TE-JT hybrid microcooler; (b) 83 K microcooler with parallel two-stage expansion; (c) 30 K two-stage microcooler.

cryocooler, of which the components of flow splitter, condenser, and restriction and evaporator were micromachined, whereas the heat exchangers still were glass tubes. All the three micromachined components were glued together with tube-in-tube CFHXs to form a whole cryocooler. They combined the semimicromachined cryocooler with a sorption compressor and in that way produced a closed-cycle cooling system. The cryocooler operated with ethylene gas and had a cooling power of about 200 mW at 169 K, when it was precooled to 238 K with a TE cooler [11,90]. After that, micromachining technology was further explored at University of Twente and fully micromachined cryocoolers based on different cooling cycles were designed through modeling and realized by using micromachining technology only.

Lerou *et al.* optimized single-stage microcoolers for maximum performance at smallest size by minimizing the entropy generation [28]. The microcoolers consisted of a stack of three wafers (see Fig. 16). The high- and low-pressure lines are etched in separate wafers with supporting pillars. These gas channels are separated by a middle wafer, thus constituting a CFHX. One end of the CFHX contains inlet and outlet ports for gas connections and the other end consists of a restriction and an evaporator. The microcoolers were made of Borosilicate glass D263T and fabricated by micromachining technology only [77]. A thin, highly reflective layer of gold was sputtered on the outer surface to minimize the parasitic heat loss caused by radiation. When the microcoolers were operated with nitrogen gas between 0.6 and 8.0 MPa, a cold-end temperature of 100 K was obtained with cooling powers in the range of 10–130 mW, depending on the size of the restriction and the cryocooler [78,91]. When these microcoolers were operated with methane gas at a low pressure of 0.4 MPa, a cold-end temperature of 140 K could be obtained. The cooling powers were in the range of 28–110 mW, depending on the high pressure, the size of the restriction and the cryocooler [91]. Compared to pure gas, mixed gases provide an equivalent cooling power with a significantly lower pressure ratio and mass-flow rate. Derking *et al.* investigated the performance of the microcooler operated

with gas mixture, driven by a linear two-stage compressor developed by the Rutherford Appleton Laboratory. When the microcooler was operated between 0.13 and 0.94 MPa with a ternary gas mixture of 39 mol% methane, 20 mol% ethane, and 41 mol% isobutene, it cooled down to below 130 K, and had a cooling power of 46 mW at 150 K [32].

Microcoolers operated with nitrogen gas required high pressures of about 8.0 MPa. Such high pressures severely add complexity to the development of compressors. To overcome this disadvantage, a TE-JT hybrid microcooler was developed [33] [see Fig. 17(a)]. The hybrid microcooler delivered an equivalent cooling power with a lower pressure or, alternatively, a higher cooling power when operating with the same pressure. It was found that the high pressure of the JT microcooler can be reduced from 8.8 to 5.5 MPa by lowering the precooling temperature from 295 to 250 K. Moreover, the effect of TE-cooler position on the performance of the hybrid microcooler was evaluated through simulation analyses.

The cold-end temperature of a JT cryocooler is determined by the exhaust pressure and the pressure drop along the low-pressure line. To reduce that pressure drop and reach a lower temperature, an 85 K microcooler with parallel two-stage expansion was developed [92] [see Fig. 17(b)]. In parallel two-stage expansion, only part of the high-pressure gas was expanded through a first restriction and returned at a relatively high temperature. The remaining gas continued to the second restriction and evaporator. Compared to the serial two-stage expansion of Little [81], the mass-flow rate through the second restriction of the cycle with parallel two-stage expansion was far less dependent of the pressure drop in the return line after the first restriction.

Cao *et al.* developed a two-stage JT microcooler operating at 30 K with modest pressures based on a stack of three wafers only [see Fig. 17(c)]. Hydrogen and neon were compared as operating fluids for reaching 30 K in the second stage, and hydrogen had a better performance [93]. The working fluid for the precooling stage was also optimized, resulting in nitrogen gas as the best choice. In the microcooler, the high- and low-pressure lines were

etched in the middle and bottom wafers. The high-pressure line ended in a flow restriction, which was extended to the evaporator volume and connected to the low-pressure line. Thus, a CFHX was formed by the high- and low-pressure channels and the thin intermediate glass wafer. In order to increase the heat transfer between precooler and the evaporator of the nitrogen stage, these were integrated into a compact design with a relatively large heat-transfer area. When the microcooler was operated with nitrogen gas between 0.1 and 8.5 MPa in the first stage and hydrogen gas between 0.1 and 7.0 MPa in the second, the two stages cooled down to about 94 and 30 K, respectively. In changing the pressure settings, the cooling power can more or less be exchanged between the two stages. These typically ranged from 21 to 84 mW at 95 K at the nitrogen stage, corresponding to 30 to 5 mW at 31–32 K at the hydrogen stage [94].

The miniaturization of JT cryocoolers results in various interesting challenges. One of these is the deposition of ice at the surfaces in the channels formed from water vapor that is present in the working fluid. Ice forms and at some moment may clog the cryocooler channels. The mechanism of clogging was investigated by Lerou and Cao *et al.* through experimental observation and theoretical analysis by using a microcooler operating with nitrogen gas [95–98]. It was found that the position and the rate of the deposition of water molecules in the microcooler mainly depend on both the inlet partial pressure of water and the temperature profile along the microcooler. During the cool-down process, the JT restriction first cooled down to cryogenic temperatures and water molecules deposited inside it. As the microcooler reached the cold-end temperature, the main deposition area shifted into the CFHX. Three measures were proposed to reduce the clogging rate: decreasing the water fraction in the supply gas using a getter filter; trapping most of the water molecules in the CFHX by decreasing the temperature gradient along the restriction; using a single microchannel at the JT restriction having a height-to-width ratio close to 1 instead of a number of smaller parallel channels.

Another challenge is the design of CFHXs that have a crucial influence on the overall behavior performance of microcoolers. Cao *et al.* investigated the flow and the heat-transfer characteristics of CFHXs with truncated cone-shaped pillar arrays [40]. A staggered arrangement of the pillars was chosen in the high-pressure channel of CFHXs to increase the heat-exchanger efficiency and thus the cooling power, whereas an aligned arrangement of the pillars was adopted in the low-pressure channel of CFHXs to reduce the pressure drop and thus lower the cold-end temperature. Besides the pillar arrays, it was found that flow maldistribution, especially those with phase change, can adversely affect the microcooler performance. Cao *et al.* revealed that the flow maldistribution was caused by the nonuniform heat-load distribution along the microcooler

and the flow maldistribution was further amplified by the Joule-Thomson cooling effect [99]. It was suggested to place devices to be cooled on a piece of silicon that was thermally connected to the cold end of the microcooler, in order to achieve a uniform heat-load distribution.

The application potentials of a microcooler coupled with electronic devices has been demonstrated by cooling an yttrium barium copper oxide film through its superconducting phase transition by using a 30 K two-stage microcooler [100]. The utilization of the microcooler in cooling a low noise amplifier (LNA) was investigated by using a 115 K single-stage microcooler [101]. The performance of an antenna system can be improved by cooling the LNA stage in order to reduce its noise figure. By cooling the LNA from 295 to 115 K, the average noise figure decreases from 0.83 to 0.50 dB, which implied that the active area of a telescope with certain sensitivity can be reduced about 43% by using JT microcooling. Kalabukhov *et al.* demonstrated a 75 K microcooler can be successfully utilized for cooling a bicrystal high-T_C SQUID gradiometer in shielded magnetic environment. Further optimization of the open-cycle microcooling system includes the elimination of additional wire resistance and electromagnetic interference from the miniature membrane pump in the control unit. Moreover, the gas cylinder in the open-cycle loop is expected to be replaced by a miniature gas compressor in order to realize a closed-cycle microcooling system [9].

3. NIST and University of Colorado

In 2006, NIST and the University of Colorado (CU), initiated a collaborative effort to develop a closed-cycle microcooler, which was designed to deliver a cooling power of about 9 mW at or near 80 K with less than 270 mW of input power to the compressor [102]. In those developments, Lin *et al.* [103] reported a microcooler operating with a five-component mixture (14 mol% propane, 16 mol% ethane, 22 mol% methane, 42 mol% nitrogen, and 6 mol% neon). The CFHX of that microcooler was formed by six hollow-core glass fibers with inner and outer diameters of 75 and 125 μm placed in a fiber with inner and outer diameters of 536 and 617 μm. This tube-in-shell-type heat exchanger had a length of 25 mm (see Fig. 18). The CFHX was solder bonded to a silicon cold end with an area of 2 mm^2. With a precooling temperature of 240 K, the cold head reached a transient temperature of 76 K and a stable temperature of 140 K with low and high pressures of 0.07 and 1.4 MPa, delivered by a macroscale compressor.

Of the same team, Lewis *et al.* [104] demonstrated a microcooler coupled with a miniature compressor for cooling to 200 K, using a hydrocarbon mixture (8 mol% methane, 46 mol% ethane, 14 mol% propane, 4 mol% butane, 26 mol% pentane) as refrigerant. The compressor
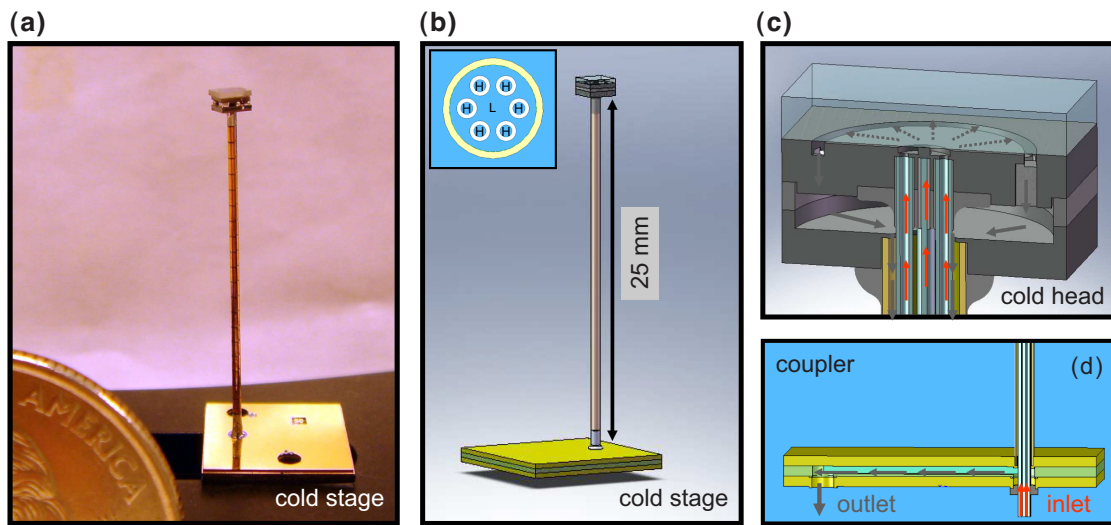
FIG. 18. NIST microcooler (adapted from Ref. [103]). (a) Photo of the cold stage; (b) sschematic of the cold stage; (c) cross section of JT valve; and (d) coupler showing the path of warm high-pressure refrigerant (red) as it expands to a lower pressure and cools (gray).

was a miniature compressor formed by coupling a piston oscillator with a micromachined check-valve assembly. The miniature compressor had a diameter of 2.5 cm and a length of 6.5 cm [105]. The linear and volume displacements are 3 mm and 0.3 ml, respectively. With a high pressure of 0.51 MPa and a low pressure of 0.1 MPa, the microcooler cooled down from 295 to 200 K in stable operation, and 166 K in transient. To investigate the temperature instabilities, Bradley *et al.* [106] compared the performance of the microcooler to that of a mesocooler. In comparison, the mesocooler was designed for the same working fluid with a mass-flow rate of about 3 to 5 times that of the microcoolers. The mesocooler demonstrated fluctuations in mass-flow rate that gave rise to temperature fluctuations of a few Kelvin but remained very stable at a low temperature of about 170 K. The results suggested that the mesoscale cryocooler did present opportunities for characterizing and validating mixed refrigerants for a microcooler. However, the temperature instabilities of a microcooler can also be caused by flow oscillations caused by liquid plugs in the high-pressure line [107], which need to be further investigated.

Wang *et al.* developed a polymer-based planar microcooler, which contained a polymer heat exchanger and a silicon and glass JT restriction [108,109]. Combined with a miniature compressor developed by Lewis *et al.* [104], the microcooler reached a 233 K stable temperature when it was operated with the hydrocarbon mixture (8 mol% methane, 46 mol% ethane, 14 mol% propane, 4 mol% butane, 26 mol% pentane) between 0.15 and 0.7 MPa. Wang *et al.* [110,111] improved their design and realized a monolithic polymer microcooler, in which the heat exchanger and the restriction were both fabricated

monolithically on a wafer all using polyimide (see Fig. 19). In contrast to the assembly-based microcooler, this monolithic polyimide microcooler did not encounter mechanical leakage problems. Using the same hydrocarbon mixture as given in the literature [108,109], the cold-end temperatures were reduced from 233 to 190 K.

In order to minimize the required pressures and to eliminate the problem of pulsating flow and temperature oscillations due to the use of mixed refrigerants, a five-stage cascaded cryocooler design was proposed by
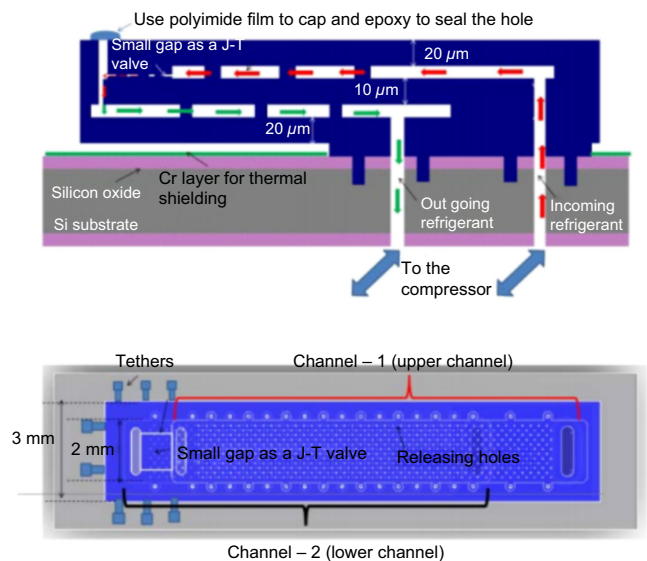

FIG. 19. Cross-section view and the top view of the monolithic polyimide microcooler developed by NIST and CU (adapted from Ref. [111]).

Radebaugh [112]. The initial theoretical thermodynamic analysis showed that a temperature of 145 K could be achieved through cascading five stages and pressure ratios of around 4. A preliminary layout for a five-stage, double-layer cold head for a net refrigeration power of 350 mW at 150 K was presented in Ref. [113]. Based on the proposal of Radebaugh [112], Coolidge [114] designed, fabricated, and characterized a two-stage cascaded microcooler and a three-stage cascaded microcooler. The two-stage microcooler was operated with isobutene and propane between 0.1 and 0.4 MPa, providing a cooling power of 150 mW at 228 K, whereas the three-stage microcooler was operated with isobutene, propane and R116 between 0.5 and 0.1 MPa, providing a cooling power of 15 mW at 193 K.

4. University of Michigan and University of Wisconsin

Zhu *et al.* reported a 1×1 cm^2 lithography-based recuperative heat exchanger for use with JT cryocoolers, in which numerous silicon plates were fabricated and stacked alternating with glass spacers [115,117] (see Fig. 20). The design was similar to the recuperative heat exchanger for turbo-Brayton cryocoolers developed by Hill *et al.* at Creare [118]. The thicknesses of the silicon plate and the glass spacer were 500 and 300 μm, respectively. The silicon plate had two rows of opening slots as high- and low-pressure channels. The slot had a width of 50 μm, a length of 1400 μm and a gap between each slot of 50 μm. White *et al.* presented a numerical modeling technique for this lithography-based heat exchanger, which was experimentally validated [119]. Park *et al.* [116] developed
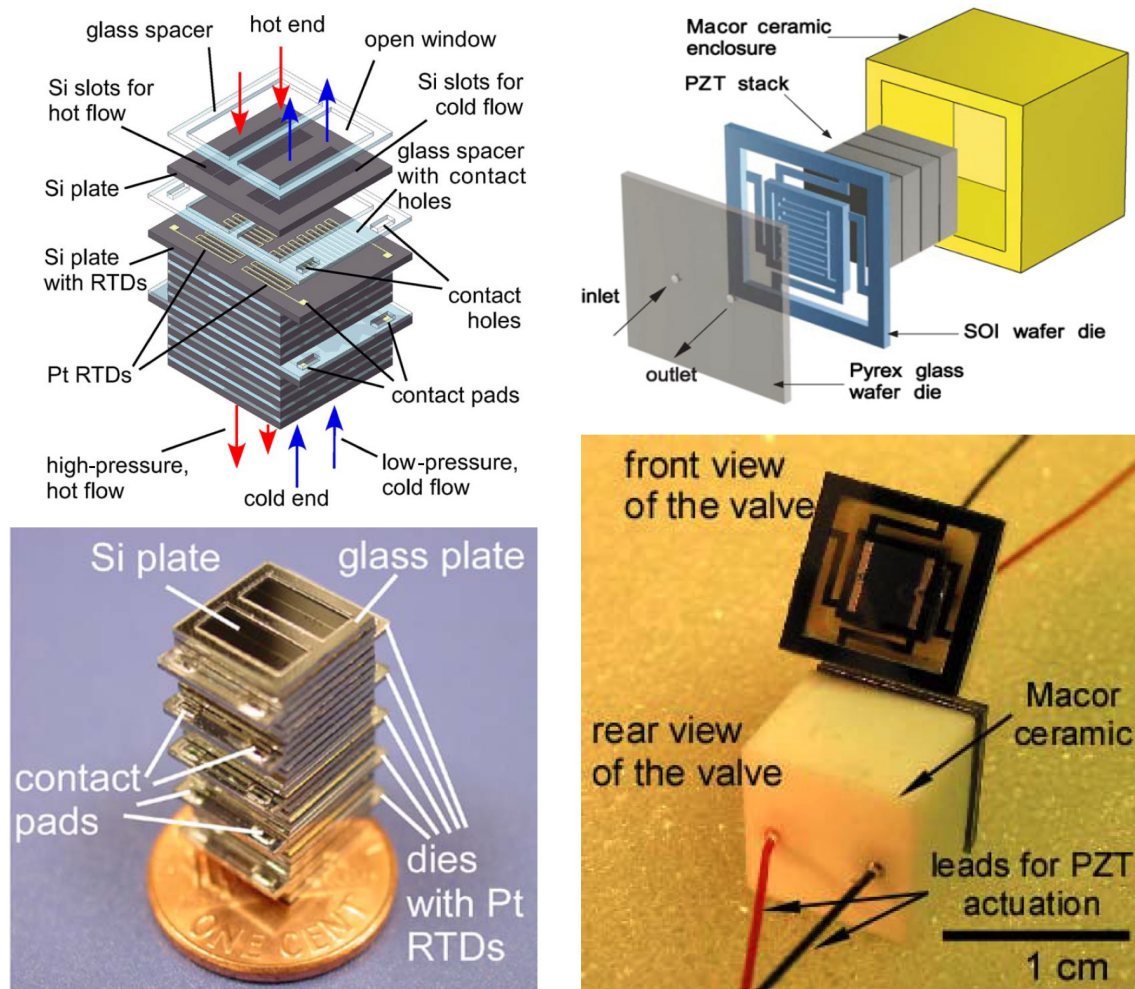

FIG. 20. Schematic (top left) and photograph (bottom left) of the perforated-plate heat-exchanger design 1×1 cm^2 (adapted from Ref. [115]). The thickness of the Si plate in each die is 500 μm. The thickness of the Pyrex spacer is 300 μm. Schematic (top right) and photograph (bottom right) of the microvalve (adapted from Ref. [116]). The microvalve consists of a ceramic-PZT (lead zirconate titanate)-Si-glass structure. PZT stack actuator moves the silicon plate to open or close the valve. Microgroove patterns are fabricated on the silicon plate to increase the flow area.

a piezoelectrically actuated microvalve with dimensions of $1 \times 1 \times 1$ cm^3 for flow modulation at cryogenic temperatures at University of Michigan and University of Wisconsin. Zhu *et al*. [120] used this microvalve in a JT cooling system as a tunable restriction with a silicon and glass heat exchanger. The tunable JT restriction facilitated the adjustment of the cooling power during steady operation, as well as during the cool down of the microcooler. They modulated an ethane gas flow between 80 and 100 mg s^{-1} with the cryocooler operating between 0.1 and 0.53 MPa. When the restriction was fully open, the cryocooler provided cooling powers of 75 mW at 255 K and 150 mW at 258 K. The experimental cool-down time was long because of the large thermal mass of the whole system. Further improvement in the integration of the tunable restriction and the heat exchanger is still necessary to eliminate the accompanying tubing and fittings to reduce the total thermal mass.

5. Other institutes and universities

Gong *et al*. [121] introduced a closed-cycle miniature JT cryocooler driven by an oil-lubricated minicompressor with a suction volume of 1.4 cm^3 [see Fig. 21(a)]. The cryocooler with dimensions of $152 \times 19 \times 8$ mm^3 includes a plate fin micro-heat-exchanger, a JT restriction and an evaporator. The heat exchanger made of stainless steel was machined by using a wire-electrode cutting method. The height of the fin was 3 mm and 2.5 mm for the low- and high-pressure channels, respectively. The width of the fin was 0.3 mm, and the size between two fins was 0.2 mm. The miniature JT cryocooler was operated with a mixture (22.8 mol% N_2, 32.4 mol% CH_4, 6.8 mol% C_2H_6, 20.9 mol% C_3H_8, 17.2 mol% iC_4H_{10}) between 0.19 and 1.7 MPa, and it cooled down to 112 K with a cooling power

of 4 W at 118 K. Geng *et al*. designed and fabricated two miniature JT cryocoolers with a length of 200 mm [see Fig. 21(b)] [122]. The first cryocooler consisted of a stack of six layers of high- and low-pressure channels and six parallel rectangular channels were etched in each layer. The cryocooler had a cold-end temperature of 178 K when it was operated with argon between 0.1 and 7 MPa. To reduce the axial heat conduction, in the second design the walls separating the six parallel channels were replaced by pillars. The second cryocooler had a cold-end temperature of 191 K when it was operated with argon between 0.1 and 5 MPa.

Considerable research has been conducted on the miniaturization of JT cryocoolers. However, these microcoolers were mainly driven by high-pressure gas cylinders rather than by compressors. A compressor is the major bottleneck in miniaturizing a closed cycle JT cooling system [123]. Sathe *et al*. investigated the performance of a miniature rotary compressor designed and fabricated by Aspen Compressor [124]. The tested compressor had a height of 78 mm, diameter of 56 mm, weight of 0.6 kg, compressor displacement of 1.4 cm^3, maximum compression ratio of 8:1, and maximum working pressure of 2.4 MPa [125]. The Aspen compressor was recommended by Little to drive a gas mixture [10]. Lin *et al*. linked Aspen compressors in series to provide a pressure ratio of up to 20:1 and integrated this set with microcoolers [103]. Gong *et al*. [121] combined an Aspen compressor with a miniature cryocooler, thus creating a closed-cycle cooling system, in which the mixture was compressed from 0.19 to 1.7 MPa. The Aspen compressor was oil lubricated, and because the lubricant oil could cause a mixture composition shift [126] and clogging at the cold end, an oil separator was required in the cooling system. Due to the adverse effect of the lubricant oil, the research on oil-free compressors is
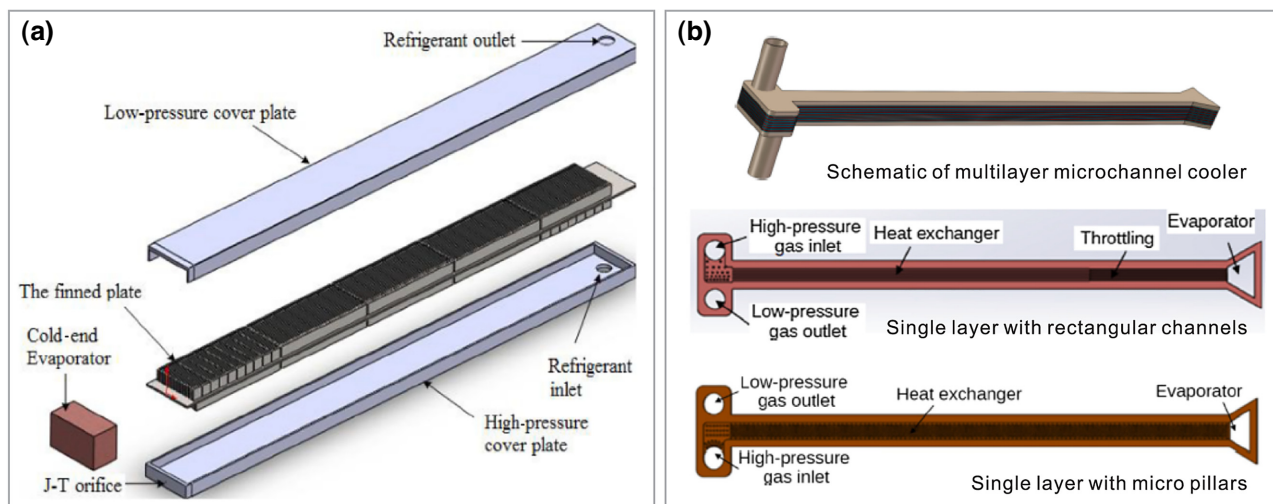

FIG. 21. (a) Schematic of Gong *et al*.'s miniature JT cryocooler (adapted from Ref. [121]). (b) Schematic of Geng *et al*.'s miniature JT cryocooler (adapted from Ref. [122]).

also being carried out. Sobol *et al.* [127] reported a miniature piezoelectric compressor, which had two compression stages and delivered a pressure ratio of 1:14.7 with a mass-flow rate of nitrogen gas of 21 mg s^{-1}. The geometry of the compressor was not given. Lewis *et al.* [128] presented a study describing the fabrication, assembly, and testing of a micro-gas-compressor. The compressor was formed by lithography-based check valves coupled to a Kapton membrane driven by a mechanically amplified piezoelectric actuator. The compressor provided a maximum pressure ratio of 4.3:1 and a maximum volume-flow rate of air of 51 standard cm^3 min^{-1} (that is about 1 mg s^{-1}). Simon *et al.* [129] developed a piezoelectric microcompressor with a stroke of about 28 μm and a swept volume of about 2 mm^3. The microcompressor had a total volume of 10 cm^3 and produced a maximum pressure ratio of 21 with no flow. Champagne *et al.* [130] adapted a traditional ac dual-opposed piston compressor with linear drive motors to a dc compressor by using check valves. The compressor had a length of 90 mm and a weight of about 200 g, and produced a pressure ratio of 1:3 with a mass-flow rate of argon gas of 27 mg s^{-1}. Burger *et al.* [90] realized a sorption compressor by using activated carbon, and the compressor cell had a diameter of 10 mm and a length of 100 mm. The sorption compressor provided a mass-flow rate of ethylene of 0.5 mg s^{-1} between 0.2 and 1.5 MPa. Olson *et al.* [131] modified a 200-g pulse-tube microcompressor for use as a JT compressor. Two check valves were added to each compressor module in order to convert the ac pressure wave into a continuous dc flow. The compressor was capable of delivering a closed-loop dc gas flow with pressure ratios from 2:1 to as high as 5:1 with a compression efficiency of 20%–30% of the ideal compression.

All the above-mentioned compressors are not truly micromachined compressors. Yoon *et al.* [134] reported a micro-gas-compressor fabricated on silicon substrates. The compressor consisted of a compression chamber (12 mm × 12 mm × 7–12 μm), check valves (1 mm × 2 mm × 50 μm) and a silicon membrane (12 mm × 12 mm × 100 μm) where the piezoelectric actuator was installed. The compressor created the largest mass-flow rate of R123 of 0.98 g h^{-1} and a maximum pressure ratio of 1.19 with no flow. Yoon *et al.* [135] later reported a two-stage compressor with the largest mass-flow rate of R123 of 0.93 g h^{-1} and a maximum pressure ratio of 1.31 with no flow. Moreover, electrostatic micropumps were fabricated by using wafer-level fabrication techniques, which offered an opportunity that microcompressors could also be realized using similar techniques [112]. Besharatian [132] developed an electrostatically actuated 24-stage peristaltic microscale pump, which used tiny micromachined hexagonal membranes in a series configuration [see Fig. 22(a)]. The pump produced a flow rate of 0.36 ml min^{-1} and reduced the pressure in a sample chamber from 101.3 kPa to about 97 kPa. The theoretical limit on the performance of such a pump is to reduce the pressure to around 1.5 kPa. The electrostatically actuated microscale pump developed by Zhou [133] achieved 22 kPa from the atmospheric pressure of 101.3 kPa [see Fig. 22(b)]. However, the two micro-vacuum-pumps did not reach their design vacuum because of a check-valve leakage, which would be an even greater challenge in the development of a microcompressor dealing with a much higher pressure.

B. Developments on regenerative microcoolers

Unlike recuperative cycles operating with a high-pressure ratio, regenerative cryocoolers need a modest pressure ratio, which makes regenerative cryocoolers intriguing for miniaturization.
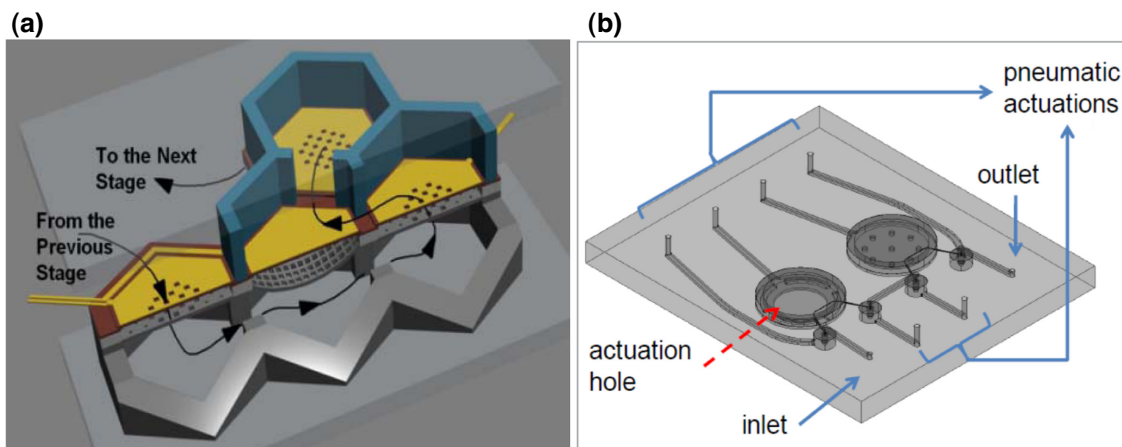

(a) **(b)**

FIG. 22.   Lithography-based compressors. (a) A 24-stage roughing pump (adapted from Ref. [132]). (b) A two-stage roughing pump with curved surfaces (adapted from Ref. [133]).

1. Miniaturization of a Stirling cryocooler

Guo *et al*. [136] proposed a conceptual MEMS-based Stirling cryocooler composed of arrays of silicon-cooling elements. Thermodynamic analysis results showed that the dead volume should be minimized, the swept volume ratio for the two chambers should be unity, and the phase lag of the volume variations between the cold side and the hot side should be 90°, in order to improve the cooling power. However, the design to date still remains a concept, due to the conduction loss through the regenerator. Maron [137] designed, optimized, and fabricated a microregenerative heat exchanger for use in a micro-Stirling device. In the design, the axial conduction was minimized by introducing many layers with low conductivity material at each interface, and with greatly reduced interfacial contact area; the pressure drop was low because of the high porosity; the heat transfer between the regenerator and the fluid was improved by using high conductivity material in each layer. Chen *et al*. [138] summarized the development of microminiature Stirling cryocoolers for high operating temperature (HOT) applications with a required temperature range of 80–200 K. They summarized that for HOT applications a rotary Stirling cryocooler is attractive because of rapid cool down and low SWaP (size, weigh, and power), whereas linear Stirling cryocoolers are more advantageous in terms of lifetime and reliability, especially at temperatures higher than 150 K. Several miniature Stirling cryocoolers have been built and commercialized in Thales [139–142] and Ricor [143–145] (see Fig. 23).

2. Miniaturization of the pulse-tube cryocooler

Xu *et al*. [150] constructed a miniature coaxial pulse-tube refrigerator using a nylon tube with an inner diameter of 5 mm and a length of 50 mm. The effective volume of the pulse-tube was about 0.4 cm^3, while the valveless compressor had a swept volume of 13.6 cm^3. The refrigerator achieved a low temperature of 159.4 K when it was operated at a frequency of 11 Hz with a filling pressure of 1.19 MPa. Nikka *et al*. [151] made a micro-double-inlet orifice pulse-tube refrigerator from glass and silicon using lithography-based technologies. A net cooling power of about 50 mW was obtained at ambient temperature when the frequency and the inflating pressure were 50 Hz and 1.2 MPa, respectively. The modest performance was mainly caused by the large heat losses due to conduction. Yaron *et al*. [152,153] designed an etched-foil regenerator for pulse-tube cryocoolers, which was fabricated from a single piece of foil. Slits were etched into the foil in precise patterns, producing well-defined flow channels. These slits interrupted the flow that was perpendicular to the slits, enhancing the heat transfer between the flow and the foil. These slits also interrupted the conduction path, reducing the conduction loss. Vanapalli *et al*. [146,154] reported on a pulse-tube cryocooler operating at 120 Hz with 3.5-MPa average pressure, which achieved a no-load temperature of about 50 K. The cryocooler cooled down to 80 K within 5.5 min and had a cooling power of 3.35 W at 80 K [see Fig. 24(a)]. Garaway *et al*. [155,156] further developed a miniature 150-Hz pulse-tube cryocooler. The cryocooler with 5.0-MPa filling pressure achieved the lowest temperature of 97 K and a cooling power of 530 mW at 120 K. Chan *et al*. [147,157] realized a compact pulse-tube cryocooler and the cryocooler provided 1.0-W cooling at 55 K and 2.5 W at 80 K with an input power of 51 W [see Fig. 24(b)]. Petach *et al*. [148] designed a coaxial pulse-tube microcooler operating at frequencies of 100–124 Hz and the microcooler had a cooling power of 1.3 W at 77 K with an input power of 50 W [see Fig. 24(c)]. Sobol and Grossman developed two miniature 113-Hz pulse-tube cryocoolers integrated with a resonant piezoelectric compressor and an inertance tube or a passive warm expander. With a filling pressure of 4.0 MPa and a pressure ratio of 1.3, the two cryocoolers cooled down from 295 to 108.7 K in about 2 min and provided cooling power of 400 mW at 110 K [158,159]. Aiming at extending the life time of cryocoolers for space applications, Lockheed [149,160–167] built three types of pulse-tube
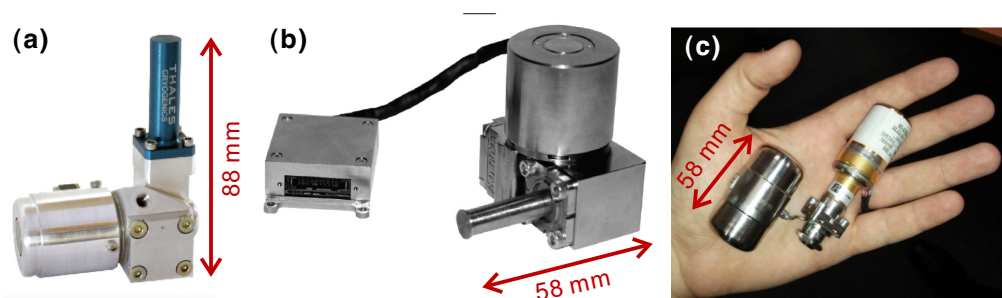

FIG. 23. Representative miniature Stirling cryocoolers. (a) Thales RM1 rotary Stirling cryocooler (100 mW @ 110 K, 2.9 W input power, 250 g, MTTF (mean time to failure): 10 000–12 000 h); (b) Ricor K580 rotary Stirling cryocooler (220 mW @ 150 K, < 2 W input power, 185 g, MTTF: 10 000–12 000 h); (c) Ricor K558 linear Stirling cryocooler (220 mW @ 150 K, < 2 W input power, 235 g, MTTF > 20 000 h).
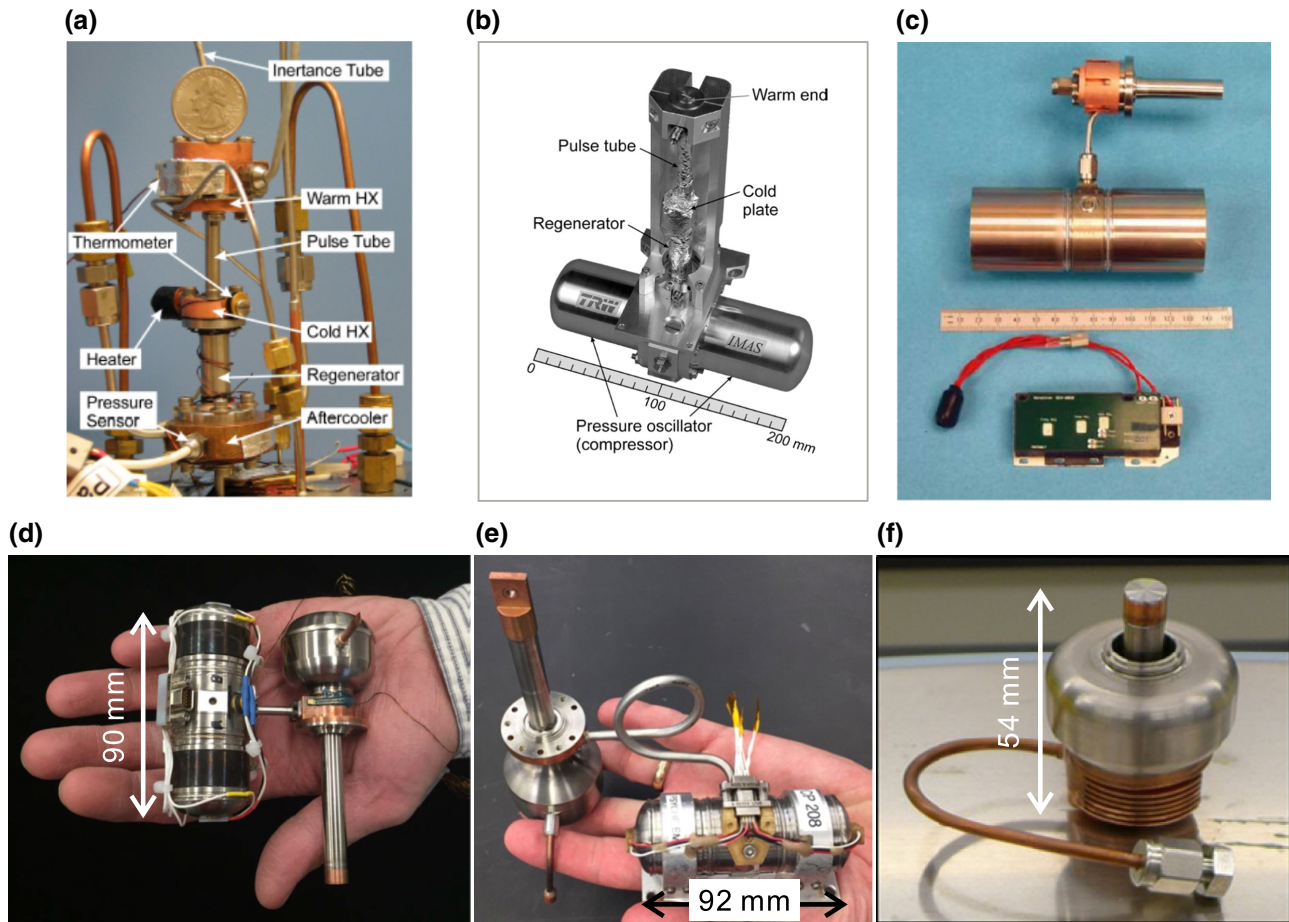
FIG. 24. Representative miniature pulse-tube cryocoolers. (a) NIST pulse-tube cold stage (3.35 W @ 80 K, 295 W input power), reproduced from [146], with the permission of AIP Publishing; (b) Northrop Grumman cryocooler (1.0 W @ 55 K, 51 W input power, 3.2 kg), reproduced from [147]; (c) TRW cryocooler (1.3 W @ 77 K, 50 W in put power, 857 g), reproduced from [148]; (d) Lockheed standard cryocooler (825 mW @ 150 K, 10 W in put power, 350 g); (e) Lockheed high-power cryocooler (2W@ 105 K, 55W in put power, 475 g); (f) Lockheed fast-cooldown cryocooler (0.3W @ 125 K, 8 W in put power, 320 g), (d)–(e) reproduced from [149] © Lockheed Martin Corporation, all rights reserved.

microcooler that were named standard microcryocooler, high-power microcryocooler, and fast-cooldown microcryocooler [see Figs. 24(d), 24(f) and 24(e)]. The standard microcryocooler with a mass of 350 g and a compressor length of 90 mm produced a cooling power of 0.825 W at 150 K when it was operated with a frequency of 94 Hz, a heat-rejection temperature of 300 K and a compressor electrical power of 10 W. This microcryocooler was qualified to TRL 6 in 2013 with launch vibration and thermal cycle testing. The high-power microcryocooler with a mass of 475 g had a cooling power of 2 W at 105 K with an input power of 55 W. This microcryocooler was qualified to TRL 6 in 2015. The fast-cooldown microcryocooler with a mass of 320 g was capable of cooling a 4.1-g copper mass to 125 K in 2.5 min with 40-W electrical power. This microcryocooler currently at TRL 5 was designed for 0.3-W cooling power at 125 K with an input power of 8 W.

Overall, miniature Stirling and pulse-tube cryocoolers have been realized by using nonlithographic micromachining technologies rather than lithographic micromachining technologies. In general, these miniature cryocoolers with a mass of a few hundreds of grams and a length of about 6 to 9 cm have cold-end temperatures higher than typically 100 K and a cooling power of a few hundred milliwatts. Compared with Stirling cryocoolers, pulse-tube cryocoolers have longer lifetime and less vibrations at the price of a lower coefficient of performance.

VI. SUMMARY AND OUTLOOK

This review discusses the opportunities and challenges that appear in the miniaturization of cryocoolers. Solid-based cooling cycles face challenges in the limits of material properties such as thermoelectric figure of merit, adiabatic magnetocaloric temperature change and

adiabatic electrocaloric temperature change, and operating conditions such as required magnetic fields and laser sources. In terms of fluid-based cooling cycles, significant progress has been made in the miniaturization of the cold stages of JT cryocoolers operating at 30–150 K. Unlike recuperative cryocoolers (especially JT cryocoolers) operating with a high-pressure ratio, regenerative cryocoolers need a modest pressure ratio, which seems to make regenerative cryocoolers more suitable for miniaturization. Miniature Stirling and pulse-tube cryocoolers operating at 100–150 K have been commercialized.

The challenges faced in the miniaturization of recuperative cryocoolers are as follows:

1. Brayton and Claude cold stages

Compared to JT cryocoolers, Brayton and Claude-cycle cryocoolers are more efficient because the use of a working-producing expander is isentropic whereas the expansion through a JT restriction is isenthalpic (and highly dissipative). However, in Brayton and Claude cryocoolers, there are moving parts in the expanders, and it is still a challenge to realize small expanders and integrate these with a heat exchanger and an evaporator, forming a miniature Brayton or Claude cryocooler.

2. Miniature compressors

At present, JT cold stages are mainly driven by high-pressure gas cylinders rather than by compressors. To make JT cooling systems practical for widespread use, miniature compressors need to be further developed. Unfortunately, the large pressure differences, which are required for JT cold stages, are probably difficult to generate with a miniature mechanical compressor. A miniature sorption compressor appears to be an attractive alternative because of the absence of mechanically moving parts.

3. Clogging phenomenon

The long-term performance of JT cold stages is limited by the clogging phenomenon caused by the deposition of water molecules present as impurity in the working fluid. Although measures to slow down the clogging rate have been proposed, how to completely eliminate this effect remains to be further investigated.

4. Gas-mixture problems

Compared to pure gas, mixed gases provide equivalent cooling power with significantly lower pressure ratio and mass-flow rate. The instability and composition shift associated with gas mixtures in microscale geometries need to be further investigated.

The challenges faced in the miniaturization of regenerative cryocoolers are as follows:

1. Regenerative cryocoolers with cold-end temperatures lower than 100 K

Commercial miniature regenerative cryocoolers can only provide a cooling temperature of 100–150 K suitable for cooling so-called hot detectors (high operation temperature, typically 150 K). Miniature regenerative cryocoolers with lower cold-end temperatures are worthy to be explored in order to broaden their application fields.

2. Batch-fabrication process

Commercial miniature regenerative cryocoolers are scaled-down versions of traditional regenerative cryocoolers, which are difficult to manufacture in batch-fabrication processes. It seems attractive to design regenerative cryocoolers in such a way that these can be batch fabricated.

3. Efficient regenerative cryocoolers

According to the analysis of the scaling effect, more efficient regenerative cryocoolers can be realized by increasing the frequency and/or the charging pressure. Meanwhile, the losses due to flow resistance in the regenerator increases as well. The realization of efficient regenerative cryocoolers is still facing challenges in the optimization of operating parameters such as cold-end temperature, frequency and charging pressure, and regenerator parameters such as material, shape, and geometry.

[1] G. Ghibaudo and F. Balestra, Low temperature characterization of silicon CMOS devices, Microelectron. Reliability **37**, 1353 (1997).

[2] A. Vassighi and M. Sachdev, *Thermal and Power Management of Integrated Circuits* (Springer, USA, 2006).

[3] S. Bhaumik and D. Kettle, Broadband X-band low noise amplifier based on 70 nm GaAs metamorphic high electron mobility transistor technology for deep space and satellite communication networks and oscillation issues, IET Microwaves, Antennas Propagation **4**, 1208 (2010).

[4] A. Rogalski and J. Piotrowski, Intrinsic infrared detectors, Prog. Quantum Electron. **12**, 87 (1988).

[5] Z. Prieskorn, C. V. Griffith, S. D. Bongiorno, A. D. Falcone, and D. N. Burrows, Characterization of Si hybrid CMOS detectors for use in the soft x-ray band, Nucl. Instrum. Methods Phys. Res. Sect. A **717**, 83 (2013).

[6] R. K. Kirschman, Low-temperature electronics, IEEE Circuits Devices Mag. **6**, 12 (1990).

[7] F. Giazotto, T. T. Heikkilä, A. Luukanen, A. M. Savin, and J. P. Pekola, Opportunities for mesoscopics in thermometry and refrigeration: Physics and applications, Rev. Mod. Phys. **78**, 217 (2006).

[8] F. Pulizzi, Squids for everything, Nat. Mater. **10**, 262 (2011).

[9] A. Kalabukhov, E. J. de Hoon, K. Kuit, P. P. P. M. Lerou, M. Chukharkin, J. F. Schneiderman, S. Sepehri, A. Sanz-Velasco, A. Jesorka, and D. Winkler, Operation of a high-T_c SQUID gradiometer with a two-stage MEMS-based Joule-Thomson micro-cooler, Supercond. Sci. Technol. **29**, 095014 (2016).

[10] W. A. Little, Microminiature refrigeration, Adv. Cryog. Eng. **53**, 597 (2008).

[11] J. Burger, Ph.D. thesis, University of Twente, Enschede, The Netherlands, 2001.

[12] R. Radebaugh, Refrigeration for superconductivities, Proc. IEEE **92**, 1719 (2004).

[13] G. Walker, R. Fauvel, and G. Reader, Miniature refrigerators for cryogenic sensors and cold electronics, Cryogenics **29**, 841 (1989).

[14] G. Walker and R. Bingham, Micro and nano cryocoolers: Speculation on future development, Cryocoolers **6**, 363 (1990).

[15] B. C. Sales, Smaller is cooler, Science **295**, 1248 (2002).

[16] V. Franco, J. S. Blazquez, B. Ingale, and A. Conde, The magnetocaloric effect and magnetic refrigeration near room temperature: Materials and models, Annu. Rev. Mater. Res. **42**, 305 (2012).

[17] B. Neese, B. Chu, S. G. Lu, Y. Wang, E. Furman, and Q. M. Zhang, Large electrocaloric effect in ferroelectric polymers near room temperature, Science **321**, 821 (2008).

[18] D. V. Seletskiy, R. Epstein, and M. Sheik-Bahae, Laser cooling in solids: Advances and prospects, Rep. Prog. Phys. **79**, 096401 (2016).

[19] E. W. Lemmon, M. L. Huber, and M. O. McLinden, Refprop version 8.0, NIST standard reference database 23 (2007).

[20] G. Walker and E. R. Bingham, *Low-Capacity Cryogenic Refrigeration* (Oxford University Press Inc., New York, 1994).

[21] R. Radebaugh, Cryocoolers: The state of the art and recent developments, J. Phys.: Condens. Matter **21**, 164219 (2009).

[22] G. Walker, *Cryocoolers Part 1: Fundamentals* (Springer, New York, USA, 1983).

[23] G. Walker, *Cryocoolers Part 2: Applications* (Springer, New York, USA, 1983).

[24] P. Kittel, Ideal orifice pulse-tube refrigerator performance, Cryogenics **32**, 843 (1992).

[25] H. Nakagome, T. Okamura, and T. Usami, Research on improvement in the efficiency of the GM refrigerator, Cryocoolers **14**, 187 (2007).

[26] M. Thirumaleshwar and S. Subramanyam, Gifford-McMahon cycle-a theoretical analysis, Cryogenics **26**, 177 (1986).

[27] A. T. A. M. de Waele, Basic operation of cryocoolers and related thermal machines, J. Low Temp. Phys. **164**, 179 (2011).

[28] P. P. P. M. Lerou, T. T. Veenstra, J. F. Burger, H. J. M. ter Brake, and H. Rogalla, Optimization of counter-flow heat exchanger geometry through minimization of entropy generation, Cryogenics **45**, 659 (2005).

[29] M. E. Will and A. T. A. M. de Waele, Heat exchanger versus regenerator: A fundamental comparison, Cryogenics **45**, 473 (2005).

[30] J. D. Denton, The 1993 IGTI scholar lecture: Loss mechanisms in turbomachines, J. Turbomach. **115**, 621 (1993).

[31] F. M. White, *Fluid Mechanics* (McGraw-Hill, New York, 2011), 7th ed.

[32] J. H. Derking, C. H. Vermeer, T. Tirolien, M. R. Crook, and H. J. M. ter Brake, A mixed-gas miniature Joule-Thomson cooling system, Cryogenics **57**, 26 (2013).

[33] H. S. Cao, S. Vanapalli, H. J. Holland, C. H. Vermeer, and H. J. M. ter Brake, Characterization of a thermoelectric/Joule-Thomson hybrid microcooler, Cryogenics **77**, 36 (2016).

[34] *Cryocomp* (a database code of the state and thermal properties for technical materials).

[35] *MPDB, Material Property Database* (https://www.jahm. com).

[36] C. K. Hsieh and K. C. Su, Thermal radiative properties of glass from 0.32 to 206 μm, Solar Energy **22**, 37 (1979).

[37] A. Bendavid, P. J. Martin, and L. Wieczorek, Morphology and optical properties of gold thin films prepared by filtered arc deposition, Thin Solid Films **354**, 169 (1999).

[38] P. Y. Wu and W. A. Little, Measurement of friction factors for the flow of gases in very fine channels used for microminiature Joule-Thomson refrigerators, Cryogenics **23**, 273 (1983).

[39] S. Vanapalli, H. J. M. ter Brake, H. V. Jansen, J. F. Burger, H. J. Holland, T. T. Veenstra, and M. C. Elwenspoek, Pressure drop of laminar gas flows in a microchannel containing various pillar matrices, J. Micromech. Microeng. **17**, 1381 (2007).

[40] H. S. Cao, S. Vanapalli, H. J. Holland, C. H. Vermeer, and H. J. M. ter Brake, Heat transfer and pressure drop in microchannels with isotropically etched pillars at sub-ambient temperatures, Int. J. Refrigeration **98**, 334 (2019).

[41] R. Radebaugh and A. O'Gallagher, Regenerator operation at very high frequencies for microcryocoolers, Adv.Cryog. Eng. **51**, 1919 (2006).

[42] H. S. Cao, C. H. Vermeer, S. Vanapalli, H. J. Holland, and H. J. M. ter Brake, Long-life micro vacuum chamber for a micromachined cryogenic cooler, J. Vacuum Sci. Technol. A **33**, 061601 (2015).

[43] J. F. O'Hanlon, *A User' s Guide to Vacuum Technology* (John Wiley & Sons, Inc., New York, 2003).

[44] D. Dornfeld, S. Min, and Y. Takeuchi, Recent advances in mechanical micromachining, CIRP Ann. **55**, 745 (2006).

[45] *ASML* (https://www.asml.com).

[46] H. Wensink, H. V. Jansen, J. W. Berenschot, and M. C. Elwenspoek, Mask materials for powder blasting, J. Micromech. Microeng. **10**, 175 (2000).

[47] R. S. Anand and K. Patra, Modeling and simulation of mechanical micro-machining: A review, Machining Sci. Technol. **18**, 323 (2014).

[48] A. Vyatskikh, S. Delalande, A. Kudo, X. Zhang, C. M. Portela, and J. R. Greer, Additive manufacturing of 3D nano-architected metals, Nat. Commun. **9**, 593 (2018).

[49] M. Elwenspoek and R. Wiegerink, in *Mechanical Microsensors* (Springer, Berlin, Heidelberg, 2001), p. 24.

[50] P. P. P. M. Lerou, Ph.D. thesis, University of Twente, Enschede, Netherlands, 2007.

[51] N. Maluf and K. Williams, *An Introduction to Microelectromechanical Systems Engineering* (Artech House, Inc., Norwood, MA, 2004), 2nd ed.

[52] H. Jansen, H. Gardeniers, M. de Boer, M. Elwenspoek, and J. Fluitman, A survey on the reactive ion etching of silicon in microtechnology, J. Micromech. Microeng. **6,** 14 (1996).

[53] H. Wensink, J. W. Berenschot, H. V. Jansen, and M. C. Elwenspoek, in *Proceedings IEEE Thirteenth Annual International Conference on Micro Electro Mechanical Systems (Cat. No.00CH36308)* (IEEE, Miyazaki, 2000), p. 769.

[54] A. G. Pawlowski, E. Belloy, A. Sayah, and M. A. M. Gijs, Powder blasting patterning technology for microfabrication of complex suspended structures in glass, Microelectron. Eng. **67–68,** 557 (2003).

[55] A. Plobl and G. Krauter, Wafer direct bonding: Tailoring adhesion between brittle materials, Mater. Sci. Eng.: R: Rep. **25,** 1 (1999).

[56] M. V. Zagarola and J. A. McCormick, High-capacity turbo-Brayton cryocoolers for space applications, Cryogenics **46,** 169 (2006).

[57] K. Saptaji, in *Handbook of Manufacturing Engineering and Technology*, edited by A. Y. C. Nee (Springer, London, 2015), p. 1089.

[58] S. Mishra and V. Yadava, Laser beam micro machining (LBMM)-a review, Opt. Lasers Eng. **73,** 89 (2015).

[59] S. Kaierle, A. Barroi, C. Noelke, J. Hermsdorf, L. Overmeyer, and H. Haferkamp, Review on laser deposition welding: From micro to macro, Phys. Proc. **39,** 336 (2012).

[60] J. P. Davim, *Nontraditional Machining Processes* (Springer-Verlag, London, 2013).

[61] K. Dhakar and A. Dvivedi, in *Advanced Manufacturing Technologies: Modern Machining, Advanced Joining, Sustainable Manufacturing*, edited by K. Gupta (Springer, Cham, 2017), p. 249.

[62] M. S. Rasheed, Comparison of micro-holes produced by micro-EDM with laser machining, Int. J. Sci. Modern Eng. **1,** 14 (2013).

[63] I. Gibson, D. Rosen, and B. Stucker, *Additive Manufacturing Technologies* (Springer-Verlag, New York, 2015).

[64] G. B. Kim, S. Lee, H. Kim, D. H. Yang, Y. H. Kim, K. Y. S. C. S. Kim, S. H. Choi, B. J. Kim, H. Ha, S. U. Kwon, and N. Kim, Three-dimensional printing: Basic principles and applications in medicine and radiology, Korean J. Radiol. **17,** 182 (2016).

[65] T. D. Ngo, A. Kashani, G. Imbalzano, K. T. Q. Nguyen, and D. Hui, Additive manufacturing (3D printing): A review of materials, methods, applications and challenges, Compos. Part B: Eng. **143,** 172 (2018).

[66] S. Singh, S. Ramakrishna, and R. Singh, Material issues in additive manufacturing: A review, J. Manuf. Process. **25,** 185 (2017).

[67] M. A. R. Krielaart, C. H. Vermeer, and S. Vanapalli, Compact flat-panel gas-gap heat switch operating at 295 K, Rev. Sci. Instrum. **86,** 115116 (2015).

[68] S. Vanapalli, R. Keijzer, P. Buitelaar, and H. J. M. ter Brake, Cryogenic flat-panel gas-gap heat switch, Cryogenics **78,** 83 (2016).

[69] N. R. Gemmell, M. Hills, T. Bradshaw, T. Rawlings, B. Green, R. M. Heath, K. Tsimvrakidis, S. Dobrovolskiy, V. Zwiller, S. N. Dorenbos, M. Crook, and R. H. Hadfield, A miniaturized 4 K platform for superconducting infrared photon counting detectors, Supercond. Sci. Technol. **30,** 11LT01 (2017).

[70] J. Tanchon, T. Trollier, P. Renaud, J. Mullie, H. Leenders, T. Prouve, I. Charles, and T. Tirolien, Design of a flight like cryostat for 30–50 K two-stage pulse-tube cooler integration, Cryocoolers **19,** 575 (2016).

[71] J. Tanchon, T. Trollier, P. Renaud, J. Mullie, H. Leenders, T. Prouve, I. Charles, and T. Tirolien, Manufacturing and testing of a flight-like cryostat for 30–50 K two-stage pulse-tube cooler, Cryocoolers **20,** 407 (2018).

[72] S. W. Stephens, Advanced design of Joule-Thomson coolers for infra-red detectors, Infrared Phys. **8,** 25 (1968).

[73] S. Garvey, S. Logan, R. Rowe, and W. A. Little, Performance characteristics of a low-flow rate 25 mW, LN_2 Joule-Thomson refrigerator fabricated by photolithographic means, Appl. Phys. Lett. **42,** 1048 (1983).

[74] E. Mikulin, J. Shevich, T. Danilenko, N. Solovov, and V. Veselov, The miniature Joule-Thomson refrigerator, Cryogenics **32,** 17 (1992).

[75] M. Chorowski, E. Bodio, and M. Wilczek, Development and testing of a miniature Joule-Thomson refrigerator with sintered powder heat exchanger, Adv. Cryog. Eng. **39,** 1475 (1994).

[76] H. J. Holland, J. F. Burger, N. Boersma, H. J. M. ter Brake, and H. Rogalla, Miniature 10–150 mW Linde-Hampson cooler with glass-tube heat exchanger operating with nitrogen, Cryogenics **38,** 407 (1998).

[77] P. P. P. M. Lerou, G. C. F. Venhorst, C. F. Berends, T. T. Veenstra, M. Blom, J. F. Burger, H. J. M. ter Brake, and H. Rogalla, Fabrication of a micro cryogenic cold stage using MEMS-technology, J. Micromech. Microeng. **16,** 1919 (2006).

[78] P. P. P. M. Lerou, H. J. M. ter Brake, J. F. Burger, H. J. Holland, and H. Rogalla, Characterization of micromachined cryogenic coolers, J. Micromech. Microeng. **17,** 1956 (2007).

[79] W. A. Little, Microminiature refrigeration, Rev. Sci. Instrum. **55,** 661 (1984).

[80] J. G. Daunt, in *Low Temperature Physics I / Kältephysik I*, edited by S. Flügge (Springer, Berlin, Heidelberg, 1956), p. 1.

[81] R. L. Paugh, New class of microminiature Joule-Thomson refrigerator and vacuum package, Cryogenics **30,** 1079 (1990).

[82] W. A. Little and R. L. Paugh, Development of a fast cooldown JT microminiature refrigerator and vacuum package for operation of infrared focal plane arrays at 70 K, Cryocoolers **6,** 161 (1991).

[83] W. A. Little, Microminiature refrigerators for Joule-Thomson cooling of electronic chips and devices, Adv. Cryog. Eng. **35**, 1325 (1990).

[84] W. A. Little, Advances in Joule-Thomson cooling, Adv. Cryog. Eng. **35**, 1305 (1990).

[85] W. A. Little, R. Yaron, and C. Fuentes, Design and operation of a 30 K two-stage nitrogen-neon JT cooler, Cryocoolers **7**, 971 (1993).

[86] W. A. Little, Micro miniature refrigerators, Patent US4392362A (1983).

[87] H. J. M. ter Brake, J. F. Burger, and H. Rogalla, in *Proceedings of the Sixteenth International Cryogenic Engineering Conference/International Cryogenic Materials Conference*, edited by T. Haruyama, T. Mitsui, and K. Yamafuji (Elsevier Science, Oxford, 1997), p. 391.

[88] J. F. Burger, H. J. M. ter Brake, M. Elwenspoek, H. Rogalla, and R. Ross, Microcooling: Study on the application of micromechanical techniques, Cryocoolers **9**, 687 (1997).

[89] H. S. Cao, S. Vanapalli, H. J. Holland, C. H. Vermeer, H. J. M. ter Brake, P. P. P. M. Lerou, and T. Tirolien, Joule-Thomson microcooling developments at university of twente, IOP Conf. Ser.: Mater. Sci. Eng. **171**, 012064 (2017).

[90] J. F. Burger, H. J. Holland, J. H. Seppenwoolde, E. Berenschot, H. J. M. ter Brake, J. G. E. Gardeniers, M. Elwenspoek, and H. Rogalla, 165 K microcooler operating with a sorption compressor and a micromachined cold stage, Cryocoolers **11**, 551 (2002).

[91] J. H. Derking, H. J. Holland, T. Tirolien, and H. J. M. ter Brake, A miniature Joule-Thomson cooler for optical detectors in space, Rev. Sci. Instrum. **83**, 045117 (2012).

[92] H. S. Cao, S. Vanapalli, H. J. Holland, C. H. Vermeer, and H. J. M. ter Brake, A micromachined Joule-Thomson cryogenic cooler with parallel two-stage expansion, Int. J. Refrigeration **69**, 223 (2016).

[93] H. S. Cao, A. V. Mudaliar, J. H. Derking, P. P. P. M. Lerou, H. J. Holland, D. R. Zalewski, S. Vanapalli, and H. J. M. ter Brake, Design and optimization of a two-stage 28 K Joule-Thomson microcooler, Cryogenics **52**, 51 (2012).

[94] H. S. Cao, H. J. Holland, C. H. Vermeer, S. Vanapalli, P. P. P. M. Lerou, M. Blom, and H. J. M. ter Brake, Characterization of a two-stage 30 K Joule-Thomson microcooler, J. Micromech. Microeng. **23**, 065022 (2013).

[95] P. P. P. M. Lerou, H. J. M. ter Brake, H. J. Holland, J. F. Burger, and H. Rogalla, Insight into clogging of micromachined cryogenic coolers, Appl. Phys. Lett. **90**, 064102 (2007).

[96] H. S. Cao, S. Vanapalli, H. J. Holland, C. H. Vermeer, and H. J. M. ter Brake, Clogging in micromachined Joule-Thomson coolers: Mechanism and preventive measures, Appl. Phys. Lett. **103**, 034107 (2013).

[97] H. S. Cao, S. Vanapalli, H. J. Holland, C. H. Vermeer, and H. J. M. ter Brake, Sensitivity of micromachined Joule-Thomson cooler to clogging due to moisture, Phys. Proc. **67**, 417 (2015).

[98] H. S. Cao, S. Vanapalli, H. J. Holland, C. H. Vermeer, and H. J. M. ter Brake, Numerical analysis of clogging dynamics in micromachined Joule-Thomson coolers, Int. J. Refrigeration **81**, 60 (2017).

[99] H. S. Cao, S. Vanapalli, H. J. Holland, C. H. Vermeer, and H. J. M. ter Brake, Heat-triggered two-phase flow maldistribution in a micromachined cryogenic cooler, Cryogenics **106**, 103026 (2020).

[100] H. S. Cao, H. J. Holland, C. H. Vermeer, S. Vanapalli, P. P. P. M. Lerou, M. Blom, and H. J. M. ter Brake, Micromachined cryogenic cooler for cooling electronic devices down to 30 K, J. Micromech. Microeng. **23**, 025014 (2013).

[101] H. S. Cao, R. H. Witvers, S. Vanapalli, H. J. Holland, and H. J. M. ter Brake, Cooling a low noise amplifier with a micromachined cryogenic cooler, Rev. Sci. Instrum. **84**, 105102 (2013).

[102] P. E. Bradley, R. Radebaugh, M. Huber, and Y. C. Lee, Development of a mixed-refrigerant Joule-Thomson microcryocooler, Cryocoolers **15**, 425 (2009).

[103] M. H. Lin, P. E. Bradley, M. L. Huber, R. Lewis, R. Radebaugh, and Y. C. Lee, Mixed refrigerants for a glass capillary micro cryogenic cooler, Cryogenics **50**, 439 (2010).

[104] R. Lewis, M. H. Lin, Y. Wang, J. Cooper, P. Bradley, R. Radebaugh, M. Huber, and Y. C. Lee, in *Proceedings of ASME International Mechanical Engineering Congress and Exposition* Vol. 11 (ASME, Denver, 2011), p. 423.

[105] R. Lewis, Y. Wang, J. Cooper, M. M. Lin, V. M. Bright, Y. C. Lee, P. E. Bradley, R. Radebaugh, and M. L. Huber, in *Infrared Technology and Applications XXXVII*, edited by B. F. Andresen, G. F. Fulop, and P. R. Norton, International Society for Optics and Photonics (SPIE, Orlando, 2011), Vol. 8012, p. 80122H.

[106] P. Bradley, R. Radebaugh, R. J. Lewis, M. H. Lin, and Y. C. Lee, Temperature instability comparison of micro- and mesoscale Joule-Thomson cryocoolers employing mixed refrigerants, AIP Conf. Proc. **1434**, 690 (2012).

[107] R. Lewis, Y. Wang, H. Schneider, Y. C. Lee, and R. Radebaugh, Study of mixed refrigerant undergoing pulsating flow in micro coolers with pre-cooling, Cryogenics **57**, 140 (2013).

[108] Y. D. Wang, R. Lewis, M. H. Lin, R. Radebaugh, and Y. C. Lee, in *IEEE 25th International Conference on Micro Electro Mechanical Systems (MEMS)* (IEEE, Paris, 2012), p. 341.

[109] Y. Wang, R. Lewis, M. H. Lin, R. Radebaugh, and Y. C. Lee, The development of polymer-based planar microcryogenic coolers, J. Microelectromech. Syst. **22**, 244 (2013).

[110] Y. D. Wang, R. Lewis, R. Radebaugh, and Y. C. Lee, in *Transducers Eurosensors XXVII: The 17th International Conference on Solid-State Sensors, Actuators and Microsystems* (IEEE, Barcelona, 2013), p. 1903.

[111] Y. Wang, R. Lewis, R. Radebaugh, M. M. Lin, V. M. Bright, and Y. Lee, A monolithic polyimide micro cryogenic cooler: Design, fabrication, and test, J. Microelectromech. Syst. **23**, 934 (2014).

[112] R. Radebaugh, Thermodynamic analysis of cascade microcryocoolers with low pressure ratios, AIP Conf. Proc. **1573**, 132 (2014).

[113] R. Radebaugh, P. Bradley, C. Coolidge, R. Lewis, and Y. C. Lee, Design and analysis of a 150 k cascade Joule-Thomson microcooler, Cryocoolers **18**, 377 (2014).

[114] C. J. Coolidge, Ph.D. thesis, University of Colorado, Colorado, United States, 2019.

[115] W. Zhu, M. J. White, G. F. Nellis, S. A. Klein, and Y. B. Gianchandani, A Si/glass bulk-micromachined cryogenic heat exchanger for high heat loads: Fabrication, test, and application results, J. Microelectromech. Syst. **19**, 38 (2010).

[116] J. M. Park, R. P. Taylor, A. T. Evans, T. R. Brosten, G. F. Nellis, S. A. Klein, J. R. Feller, L. Salerno, and Y. B. Gianchandani, A piezoelectric microvalve for cryogenic applications, J. Micromech. Microeng. **18**, 015023 (2007).

[117] W. Zhu, M. J. White, G. F. Nellis, S. A. Klein, and Y. B. Gianchandani, in *IEEE 21st International Conference on Micro Electro Mechanical Systems* (IEEE, Tucson, 2008), p. 844.

[118] R. Hill, M. Izenson, W. Chen, and M. Zagarola, A recuperative heat exchanger for space-borne turbo-brayton cryocoolers, Cryocoolers **14**, 525 (2007).

[119] M. White, G. Nellis, S. Kelin, W. Zhu, and Y. Gianchandani, An experimentally validated numerical modeling technique for perforated plate heat exchangers, J. Heat Transfer **132**, 1 (2010).

[120] W. Zhu, J. M. Park, M. J. White, G. F. Nellis, and Y. B. Gianchandani, Experimental evaluation of an adaptive Joule-Thomson cooling system including silicon-microfabricated heat exchanger and microvalve components, J. Vacuum Sci. Technol. A **29**, 021005 (2011).

[121] M. Q. Gong, J. F. Wu, B. Yan, X. Zou, X. R. Zhuang, and Q. G. Hu, Study on a miniature mixed-gases Joule-Thomson cooler driven by an oil-lubricated mini-compressor for 120 K temperature ranges, Phys. Proc. **67**, 405 (2015).

[122] H. Geng, X. Cui, J. Weng, H. She, and W. Wang, Review of experimental research on Joule-Thomson cryogenic refrigeration system, Appl. Therm. Eng. **157**, 113640 (2019).

[123] S. Jeong, How difficult is it to make a micro refrigerator? Int. J. Refrigeration **27**, 309 (2004).

[124] A. Sathe, E. Groll, and S. Garimella, in *Proceedings of the International Compressor Engineering Conference* (Purdue University, Purdue, 2008), p. 1115.

[125] *Aspen Compressor* (https://www.asml.com).

[126] M. Gong, W. Zhou, and J. Wu, Composition shift due to the different solubility in the lubricant oil for multicomponent mixtures, Cryocoolers **14**, 459 (2007).

[127] S. Sobol, N. Tzabar, and G. Grossman, Miniature piezoelectric compressor for Joule-Thomson cryocoolers, Phys. Proc. **67**, 423 (2015).

[128] R. Lewis, C. J. Coolidge, P. J. Schroeder, V. M. Bright, and Y. C. Lee, Fabrication, assembly, and testing of a MEMS-enabled micro gas compressor for a 4:1 pressure ratio, Sens. Actuators A: Phys. **190**, 84 (2013).

[129] M. J. Simon, C. DeLuca, V. M. Bright, Y. C. Lee, P. E. Bradley, and R. Radebaugh, Development of a piezoelectric microcompressor for a Joule-Thomson microcryocooler, Cryocoolers **15**, 441 (2009).

[130] P. Champagne, J. R. Olson, T. Nast, E. Roth, A. Collaco, G. Kaldas, E. Saito, and V. Loung, Development of a JT micro compressor, IOP Conf. Ser.: Mater. Sci. Eng. **101**, 012009 (2015).

[131] J. R. Olson, E. Roth, M. Guzinski, A. Ruiz, C. L. Mangun, D. King, N. Hejmanowski, and D. L. Carroll, Joule-Thomson microcryocooler test results, Cryocoolers **20**, 287 (2018).

[132] A. Besharatian, K. Kumar, R. L. Peterson, L. P. Bernal, and K. Najafi, in *IEEE 25th International Conference on Micro Electro Mechanical Systems (MEMS)* (IEEE, Paris, 2012), p. 1001.

[133] H. Zhou, H. Q. Li, V. Sharma, and M. A. Schmidt, in *Proceedings of IEEE 24th International Conference on Micro Electro Mechanical Systems* (IEEE, Cancun, 2011), p. 1095.

[134] J. S. Yoon, J. W. Choi, and M. S. Kim, Computational and experimental investigation on the performance characteristics of the micro gas compressor, Microelectron. Eng. **86**, 1975 (2009).

[135] J. S. Yoon, J. W. Choi, M. S. Kim, Y. E. Yoo, and D. S. Choi, Studies on the performance characteristics and improvements of the piezoelectrically-driven micro gas compressors, Microelectron. Eng. **86**, 2297 (2009).

[136] D. Guo, J. Gao, A. J. H. McGaughey, M. Moran, S. Santhanam, G. K. Fedder, B. Anderson, and S.-C. Yao, in *Proceedings of the ASME International Mechanical Engineering Congress and Exposition* Vol. 4 (ASME, Denver, 2011), p. 83.

[137] M. Moran, S. Stelter, and M. Stelter, in *CANEUS 2004 Conference on Micro-Nano-Technologies* (AIAA, Monterey, 2004), p. NASA/TM–2004–213353.

[138] X. P. Chen, H. Sun, X. L. Nie, and Z. H. Gan, Overview of micro-miniature stirling cryocoolers for high temperature applications, Cryocoolers **19**, 287 (2016).

[139] J. Y. Martin, S. Freche, R. Griot, and T. Benschop, in *Infrared Technology and Applications XXXVII*, edited by B. F. Andresen, G. F. Fulop, and P. R. Norton, International Society for Optics and Photonics (SPIE, Orlando, 2011), Vol. 8012, p. 80122L.

[140] C. Vasse, J. Y. Martin, C. Seguineau, and T. Benschop, Miniaturization of rotary stirling cryocoolers, Cryocoolers **20**, 63 (2018).

[141] C. Vasse, C. Seguineau, J. Y. Martin, S. Van-Acker, M. Sacau, J. L. Bordays, T. Etchanchu, C. Abadie, S. Chaumeau, and T. Benschop, in *Tri-Technology Device Refrigeration (TTDR) III*, edited by M. Sheik-Bahae, R. I. Epstein, B. F. Andresen, T. Benschop, J. P. Heremans, and S. V. Riabzev, International Society for Optics and Photonics (SPIE, Orlando, 2018), Vol. 10626, p. 1062605.

[142] C. Vasse, J. Y. Martin, J. M. Cauquil, G. Raynal, and T. Benschop, in *Infrared Technology and Applications XLV*, edited by B. F. Andresen, G. F. Fulop, and C. M. Hanson, International Society for Optics and Photonics (SPIE, Baltimore, 2019), Vol. 11002, p. 110020A.

[143] A. Veprik, S. Zechtzer, N. Pundak, S. Riabzev, C. Kirckconnel, and J. Freeman, Low cost split stirling cryogenic cooler for aerospace applications, AIP Conf. Proc. **1434**, 1465 (2012).

[144] D. L. Johnson, M. J. Lysek, and J. M. Morookian, The Ricor K508 cryocooler operational experience on mars, AIP Conf. Proc. **1573**, 1792 (2014).

[145] O. B. David, M. Carmiel, V. Segal, I. Vainshtein, S. Riabzev, and A. Filis, in *Infrared Technology and Applications XLV*, edited by B. F. Andresen, G. F. Fulop, and C. M. Hanson, International Society for Optics and Photonics (SPIE, Baltimore, 2019), Vol. 11002, p. 110022M.

[146] S. Vanapalli, M. Lewis, G. Grossman, Z. Gan, R. Radebaugh, and H. J. M. ter Brake, Modeling and experiments on fast cooldown of a 120 Hz pulse-tube cryocooler, AIP Conf. Proc. **985**, 1429 (2008).

[147] R. Radebaugh, in *Infrared Technology and Applications XXVI*, edited by B. F. Andresen, G. F. Fulop, and M. Strojnik, International Society for Optics and Photonics (SPIE, San Diego, 2000), Vol. 4130, p. 363.

[148] M. Petach, M. Waterman, G. Pruitt, and E. Tward, High frequency coaxial pulse-tube microcooler, Cryocoolers **15**, 97 (2009).

[149] J. R. Olson, in *33rd Annual AIAA/USU Conference on Small Satellites* (Lockheed Martin Corporation, Palo Alto, 2019), p. SSC19–VII–04.

[150] M. Xu, Y. He, P. Wu, and Z. Chen, Experimental research of a miniature coaxial pulse-tube refrigerator using nylon tube, Cryogenics **36**, 131 (1996).

[151] P. Nika, Y. Bailly, J. C. Jeannot, and M. D. Labachelerie, An integrated pulse-tube refrigeration device with micro exchangers: Design and experiments, Int. J. Thermal Sci. **42**, 1029 (2003).

[152] R. Yaron and M. P. Mitchell, Foil regenerator, Patent US5429177A (1995).

[153] R. Yaron, S. Shokralla, J. Yuan, P. E. Bradley, and R. Radebaugh, Etched foil regenerator, Adv. Cryog. Eng. **41**, 1339 (1996).

[154] S. Vanapalli, M. Lewis, Z. Gan, and R. Radebaugh, 120 Hz pulse-tube cryocooler for fast cooldown to 50 K, Appl. Phys. Lett. **90**, 072504 (2007).

[155] I. Garaway, Z. Gan, P. Bradley, A. Veprik, and R. Radebaugh, Development of a miniature 150 hz pulse-tube cryocooler, Cryocoolers **15**, 105 (2009).

[156] R. Radebaugh, I. Garaway, and A. Veprik, in *Proceedings of SPIE-The International Society for Optical Engineering* (SPIE, Orlando, 2010), Vol. 7660, p. 76602J.

[157] C. K. Chan, T. Nguyen, R. Colbert, J. Raab, R. G. Ross, and D. L. Johnson, IMAS pulse-tube cooler development and testing, Cryocoolers **10**, 139 (2002).

[158] Y. K. S. Sobol and G. Grossman, A study of a miniature in-line pulse-tube cryocooler, Cryocoolers **16**, 87 (2011).

[159] S. Sobol and G. Grossman, Miniature PT cryocooler activated by resonant piezoelectric compressor and passive warm expander, IOP Conf. Ser.: Mater. Sci. Eng. **278**, 012141 (2017).

[160] J. R. Olson, P. Champagne, E. W. Roth, G. B. Kaldas, E. S. T. Nast, V. Loung, B. S. McCay, A. C. Kenton, and C. L. Dobbins, Coaxial pulse-tube microcryocooler, Cryocoolers **18**, 51 (2014).

[161] J. R. Olson, P. Champagne, E. Roth, T. Nast, E. Saito, V. Loung, A. C. Kenton, and C. L. Dobbins, Microcryocooler for tactical and space applications, AIP Conf. Proc. **1573**, 357 (2014).

[162] T. C. Nast, E. Roth, J. R. Olson, P. Champagne, and D. Frank, Qualification of Lockheed Martin micro pulse-tube cryocooler to trl6, Cryocoolers **18**, 45 (2014).

[163] J. R. Olson, G. Kaldas, P. Champagne, E. Roth, and T. Nast, MatlSSE microcryocooler, IOP Conf. Ser.: Mater. Sci. Eng. **101**, 012025 (2015).

[164] I. M. McKinley, D. L. Johnson, and J. I. Rodriguez, Characterization testing of Lockheed Martin standard micro pulse-tube cryocooler, Cryocoolers **19**, 75 (2016).

[165] I. M. McKinley, C. D. Hummel, D. L. Johnson, and J. I. Rodriguez, Characterization testing of Lockheed Martin high-power micro pulse-tube cryocooler, IOP Conf. Ser.: Mater. Sci. Eng. **278**, 012007 (2017).

[166] J. R. Olson, E. W. Roth, L.-S. Sanders, E. Will, and D. J. Frank, in *Tri-Technology Device Refrigeration (TTDR) II*, edited by R. I. Epstein, B. F. Andresen, T. Benschop, J. P. Heremans, S. V. Riabzev, and M. Sheik-Bahae, International Society for Optics and Photonics (SPIE, Anaheim, 2017), Vol. 10180, p. 1018004.

[167] J. R. Olson, E. Roth, E. T. Will, M. Guzinski, A. Ruiz, I. M. McKinley, D. L. Johnson, J. I. Rodriguez, and K. Frohling, Maturation and status of the Lockheed Martin micro1-2 cryocooler, Cryocoolers **20**, 81 (2018).